Supplementary Information

Ligand-field symmetry and magneto-optical correlations in a luminescent Dy(III) single-molecule magnet

Senthil Kumar Kuppusamy,[a*] Christian Pachl,[b,c] Zhaoyang Jing,[b] Sagar Paul,[d] Benoît Heinrich,[e] Olaf Fuhr,[b,f] Svetlana Klayatskaya,[b] Wolfgang Wernsdorfer,[a,d] Annie K. Powell,[a,b,c] Karin Fink,[b] and Mario Ruben [a,b,g]

[a]Institute of Quantum Materials and Technologies (IQMT), Karlsruhe Institute of Technology (KIT), Kaiserstraße 12, 76131 Karlsruhe, Germany.
E-mail: senthil.kuppusamy2@kit.edu

[b]Institute of Nanotechnology (INT), Karlsruhe Institute of Technology (KIT), Kaiserstraße 12, 76131 Karlsruhe, Germany.

[c]Institute of Inorganic Chemistry (AOC), Karlsruhe Institute of Technology (KIT), Kaiserstraße 12, 76131 Karlsruhe, Germany.

[d]Physikalisches Institut (PHI), Karlsruhe Institute of Technology (KIT), Kaiserstraße 12, 76131 Karlsruhe, Germany.

[e]Institut de Physique et Chimie des Matériaux de Strasbourg (IPCMS), CNRS-Université de Strasbourg, Strasbourg, France

[f]Karlsruhe Nano Micro Facility (KNMFi), Karlsruhe Institute of Technology (KIT), Kaiserstraße 12, 76131 Karlsruhe, Germany

[g]Centre Européen de Sciences Quantiques (CESQ) Institut de Science et d'Ingénierie, Supramoléculaires (ISIS), 8 allée Gaspard Monge, BP 70028, 67083 Strasbourg Cedex, France.

Contents

S1. Materials and methods

S1.1. Materials

All the solvents and reagents were purchased from commercial sources and used as received.

S1.2. Methods

Elemental analysis: Elemental analyses of the ligands and compounds were performed using Elementar vario MICRO cube elemental analyzer.

SC-XRD: Single-Crystal X-ray Diffraction patterns of compounds were collected employing a STOE STADIVARI diffractometer with a monochromated MoKα (0.71073 Å) radiation. A suitable crystal was selected and kept at 180 K during data collection. Using Olex2,[1] the structures were solved with the ShelXT[2] structure solution program using Intrinsic Phasing and refined with the ShelXL[3] refinement package using Least Squares minimization. Refinement was performed with anisotropic temperature factors for all non-hydrogen atoms; hydrogen atoms were calculated on idealized positions.

HR-PXRD: High-Resolution Powder X-ray Diffraction patterns were obtained with a transmission Guinier-like geometry. A linear focalized monochromatic Cu Kα1 beam (λ = 1.54056 Å) was obtained using a sealed-tube generator (600 W) equipped with a bent quartz monochromator. The samples were filled in sealed cells of adjustable path. The sample temperature was controlled within ±0.1 °C, and exposure times were of 24 h. The patterns were recorded on image plates and scanned with Amersham Typhoon IP scanner at 25 µm resolution. I(2θ) profiles were obtained from images, by using a home-developed software.

SEM and EDX studies: Measurements were performed on a Zeiss LEO 1530 Gemini microscope operated at an accelerating voltage of 5–20 kV. The samples were deposited on conductive carbon tape and coated with a thin layer of gold (Au) using a sputter coater to minimize charging effects during imaging. To complement the morphological analysis, EDX was used for elemental characterization. Elemental analysis was conducted by Oxford Instruments X-Max detector, integrated with the SEM system an accelerating voltage of 20 kV.

µ-SQUID studies: Single-crystal magnetic measurements using µSQUIDs were performed in the temperature range of 0.03–4.5 K in a dilution refrigerator. A crystal approximately 50 µm in length (along its long axis) was positioned within a few micrometres from the µSQUID loop to ensure optimal magnetic coupling, crucial while measuring magnetically diluted crystals. A 3D vector magnet enabled precise control of the magnetic field direction within the µSQUID plane, with angular accuracy better than 0.1°. This allowed identification of the magnetic easy axis, along which the measurements are presented. Low-temperature $M(H)$ measurements were conducted at various field sweep rates (0.001–0.128 T s^{-1}), with a time resolution of approximately 1 ms.

S2. Preparation, characterization, molecular structures, and phase purity of Ln(III) compounds discussed in this study

S2.1. Preparation and characterization of Ln(III) compounds—1, 1@Y, and 3

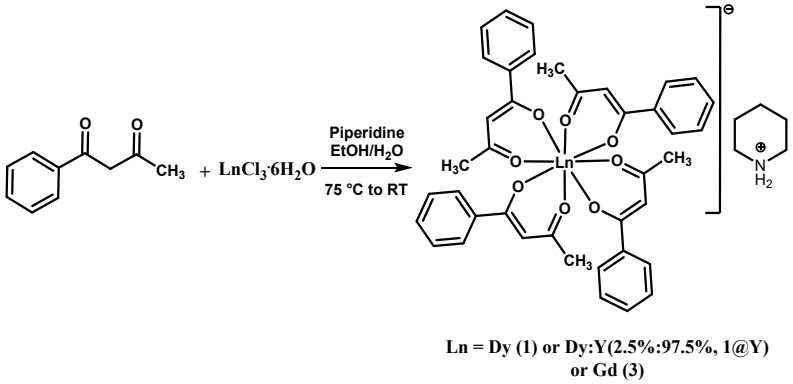

Scheme S1. Preparation of Ln(III) compounds—**1**, **1@Y**, and **3**—discussed in this study.

Preparation of compound 1: To an ethanol solution (20 ml) of 1-phenylbutane-1,3-dione (1.3 g, 8 mmol) at 75 °C, piperidine (0.8 ml, 8 mmol) was added, and the solution was stirred for 15 minutes. $DyCl_3 \cdot 6H_2O$ (754 mg, 4 mmol) dissolved in 10 ml of water was added to the pale-

yellow solution of the deprotonated ligand. The reaction mixture was stirred at 75 °C for 2 h, cooled to room temperature without stirring, and filtered. Seeding of the filtrate with a few previously prepared crystals of **1** resulted in the formation of crystals of the compound suitable for single-crystal X-ray diffraction studies. Yield: 0.680 g. Elemental analysis: Calculated for $C_{45}H_{48}DyO_8N$, C, 60.5; H, 5.42; N, 1.57. Found, C, 60.54; H, 5.56; N, 1.75.

Preparation of Y(III)-diluted version of the Dy(III) compound—1@Y: The procedure used above for compound **1** was adopted to prepare the yttrium diluted version of the Dy(III) compound using Y(III) and Dy(III) salts in 97.5: 2.5 ratio. Yield: 0.410 g. Elemental analysis of $C_{45}H_{48}Dy_{0.025}Y_{0.975}NO_8$ (2.5%-Dy): C, 65.78; H, 5.89; N, 1.70. Found, C, 65.09; H, 5.58; N, 1.78.

Preparation of compound 3: Procedure as employed for the preparation of compound **1**. $GdCl_3 \cdot 6H_2O$ (744 mg, 4 mmol) was used instead of the Dy(III) salt. Yield: 1.217 g (68.52%). Elemental analysis: Calculated for $C_{45}H_{48}DyO_8N$, C, 60.86; H, 5.45; N, 1.58. Found, C, 60.42; H, 5.10; N, 1.73.

S2.2. Single-crystal X-ray diffraction (SC-XRD) studies of compounds 1 and 3: elucidation of molecular structures

Table S1. Crystallographic data of compounds **1** and **3**.

Compound 1			
Parameter	Value	Parameter	Value
CCDC number	2010809	α/°	90
Formula	$C_{45}H_{48}DyO_8N$	β/°	106.362(1)
FW/g.mol^{-1}	893.34	γ/°	90
T/K	180	V/Å^3	4056.86(7)
Crystal System	Monoclinic	Z	4
Space group	$P2_1/n$	ρ/g.cm^{-3}	1.463
a/Å	11.6780(1)	μ/mm^{-1}	1.896
b/Å	19.6010(2)	$R1$	0.0227
c/Å	18.4713(2)	$wR2$	0.0583
Compound 3			
Parameter	Value	Parameter	Value
CCDC number	2441051	α/°	90
Formula	$C_{45}H_{48}GdO_8N$	β/°	106.550(2)
FW/g.mol^{-1}	888.09	γ/°	90
T/K	180	V/Å^3	4065.52(18)

Crystal System	Monoclinic	*Z*	4
Space group	$P2_1/n$	ρ/g.cm^{-3}	1.451
a/Å	11.7028(3)	μ/mm^{-1}	1.685
b/Å	19.5824(4)	*R1*	0.0295
c/Å	18.5070(5)	*wR2*	0.0546

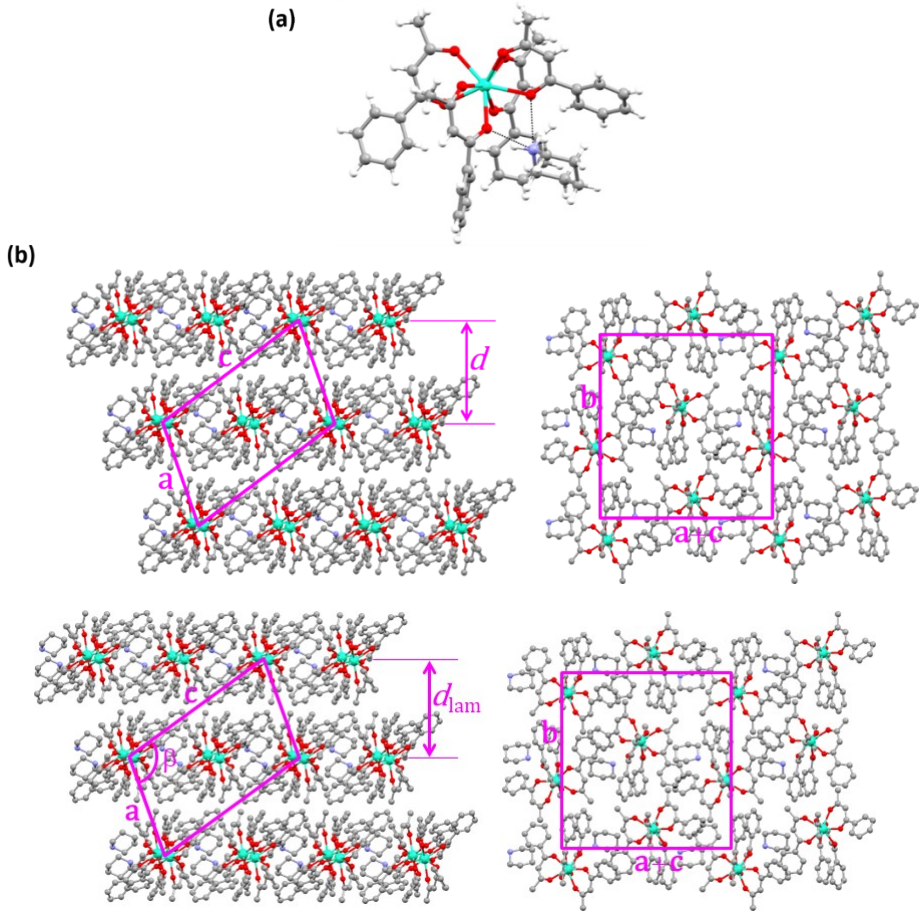

Figure S 1. Single-crystal X-ray diffraction (SC-XRD) studies. (a) Molecular structure of compound **1** obtained from the SC-XRD studies. Colour code: C, grey; Dy, teal; H, white; N, blue; O, red. The black dotted lines indicate the hydrogen bonding interactions between two of the ligands and counted cation. (b) Lamellar self-assembly in the crystal lattice of **1**. d_{lam} is the lamellar periodicity resulting from the self-assembly of the compounds into layers parallel to the **b**×(**a**+**c**) plane. The arrangement in the layer plane is rectangular with 4 molecules per lattice. The structure and molecular organization of the Gd(III) compound **3** is the same as compared with its Dy(III) counterpart; therefore, the structure and organization of compound **3** is not presented.

Table S2. Continuous shape measures (CShM) obtained for compound **1** from the SHAPE 2.1 software. The CShM values obtained for the previously reported Eu(III) compound (**2**) is shown in parenthesis.

Coordination geometry	Compound **1** (Eu(III) compound)	
	Pointgroup	CShM value
Square antiprism	D_{4d}	0.139 (0.169)
Biaugmented trigonal prism	C_{2V}	2.243 (2.268)
Triangular dodecahedron	D_{2d}	2.508 (2.484)
Biaugmented trigonal prism J50	C_{2V}	2.804 (2.826)
Snub diphenoid J84	D_{2d}	5.194 (5.230)
Cube	O_h	10.444 (10.369)
Triakis tetrahedron	T_d	11.220 (11.136)
Johnson gyrobifastigium J26	D_{2d}	16.867 (16.713)
Hexagonal bipyramid	D_{6h}	17.628 (17.600)
Heptagonal pyramid	C_{7v}	23.250 (23.020)
Elongated trigonal bipyramid	D_{3h}	23.271 (22.907)
Johnson elongated triangular bipyramid J14	D_{3h}	27.783 (27.423)
Octagon	D_{8h}	28.555 (28.599)

Table S3. Magic (α) and skew (Φ) angles associated with compounds **1** and **2**.

S. No.	α (**1**)	α (**2**)	Φ (**1**)	Φ (**2**)
1	55.64°	55.48°	47.28°	46.75°
2	57.33°	57.35°	38.12°	38.15°
3	57.38°	57.37°	46.34°	46.96°
4	57.54°	57.48°	38.82°	38.93°
5	57.61°	57.64°		
6	58.59°	58.45°		
7	58.90°	58.97°		
8	58.92°	59.00°		
Average	57.74°	57.72°	42.64°	42.69°

S2.3. High-resolution powder X-ray diffraction (HR-PXRD) studies of compound **1** and **1@Y**

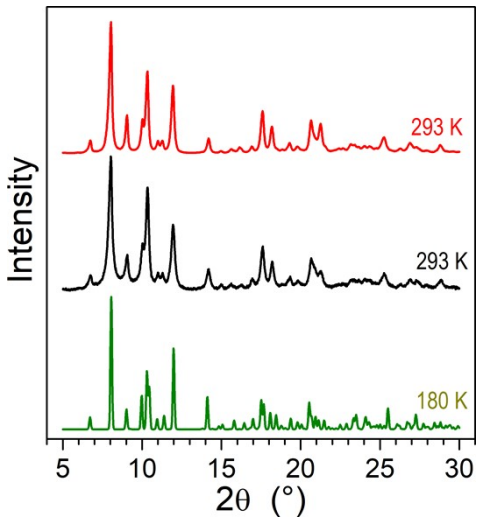

Figure S 2. HR-PXRD patterns of **1@Y** (top) and **1** (middle) as compared to the powder pattern simulated from the SC-XRD data of single-crystal of compound **1** (bottom).

Table S4. Structural parameters of **1** and **1@Y** in powder and single crystal forms.

Parameters	100% (SC-XRD)	100% (PXRD)	2.5% (PXRD)
T/K	180	293	293
a/Å	11.6780	11.796	11.798
b/Å	19.6010	19.517	19.526
c/Å	18.4713	18.313	18.320
α/°	90	90	90
β/°	106.362	105.77	105.56
γ/°	90	90	90
V/Å^3	4056.9	4057.4	4065.6
Z	4	4	4
V_{mol}/Å^{3a}	1014.22	1014.3	1016.4
d_{lam}/Å^b	10.969	11.00	10.99
a_{2D}/Å^c	18.869	18.90	18.94
A_{mol}/Å^{2d}	92.46	92.2	92.5
$\sqrt{A_{mol}}/d_{lam}$^{e}	0.876	0.873	0.875

[a] $V_{mol} = V/Z$ is the molecular volume

[b] $d_{lam} = d_{10\bar{1}}$ is the lamellar periodicity

[c] $a_{2D} = ||\mathbf{a}+\mathbf{c}|| = (V/d_{lam})/b$ and $b_{2D} = b$ are the parameters of the rectangular lattice (Z_{2D} = 4 molecules)

[d] $A_{mol} = V_{mol}/d_{lam}$ is the molecular area, i.e. the molecular layer area per molecule

[e] $\sqrt{A_{mol}}/d_{lam}$) indicates the degree of lateral spreading of the molecular layers

S3. SEM-EDX studies of compound 1@Y.

In this study, SEM and EDX were employed to characterize the elemental composition of **1@Y** crystals. EDX detects the characteristic X-rays emitted from the sample upon electron-beam excitation, allowing qualitative and semi-quantitative determination of the elemental composition. Together, SEM and EDX enable the correlation of morphological features with chemical composition, confirming the presence and distribution of expected elements in the analyzed materials. Accordingly, the SEM–EDX analysis confirms the incorporation of the Dy(III) centers within the Y(III) crystalline lattice.

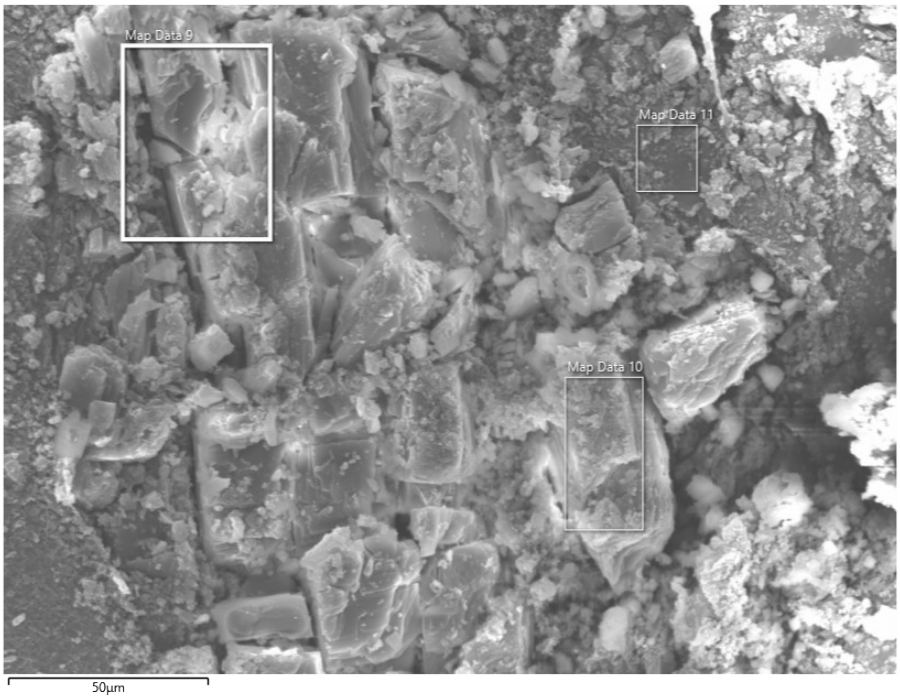

Figure S 3. SEM image of the crystallizes of the **1@Y** compound.

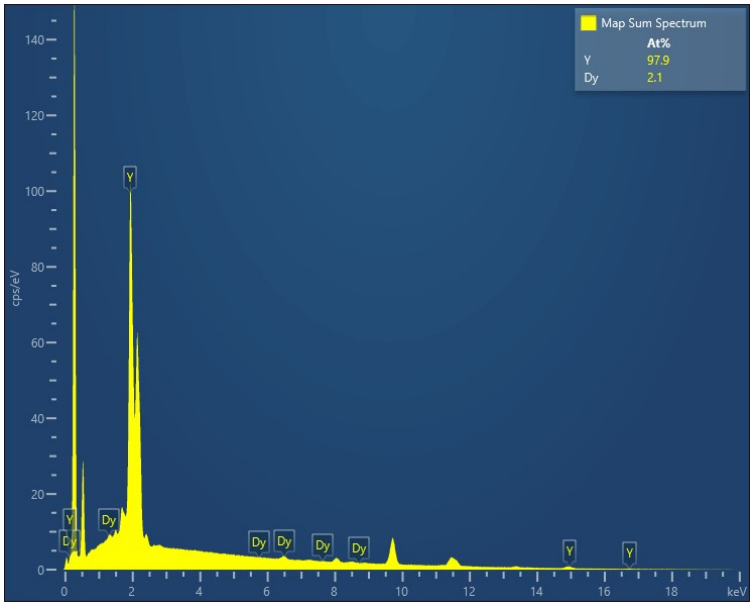

Figure S 4. EDX spectrum measured at position 9 (map data 9) in Figure S3.

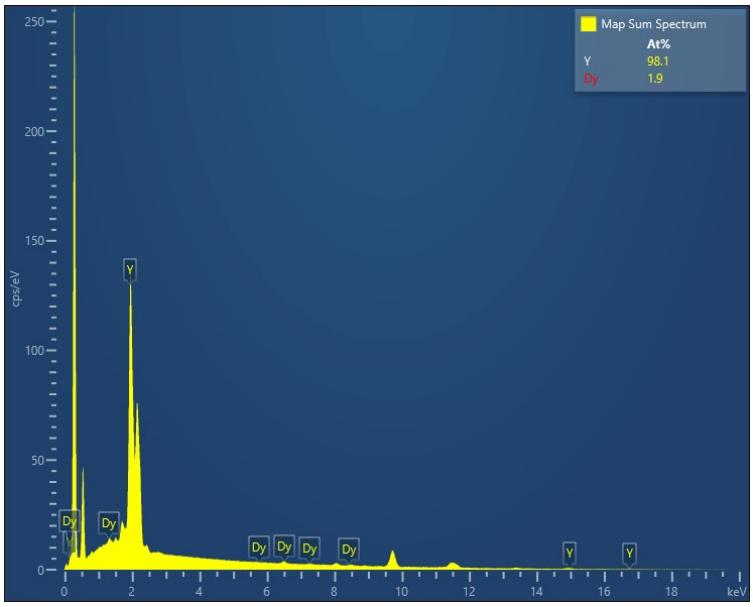

Figure S 5. EDX spectrum measured at position 10 (map data 10) in Figure S3.

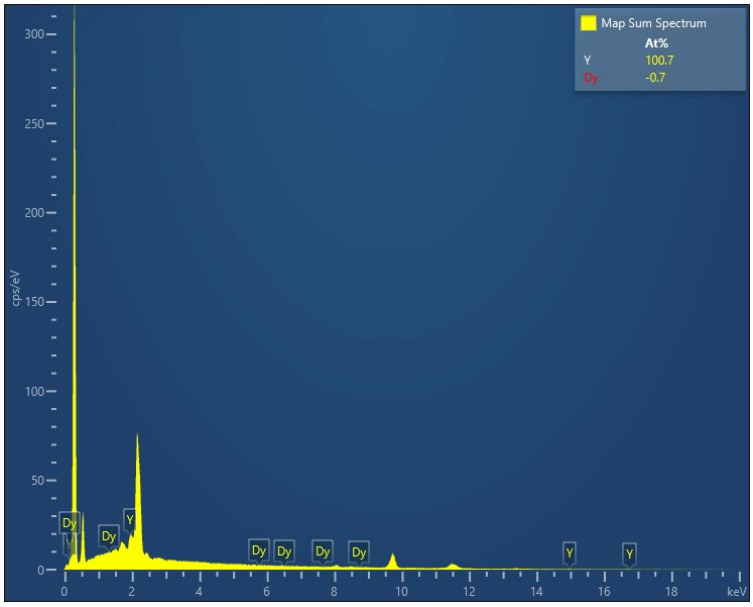

Figure S 6. EDX spectrum measured at position 11 (map data 11) in Figure S3.

S4. Magnetic properties of compounds 1 and 1@Y

S4.1. Magnetization studies of compounds 1 and 1@Y

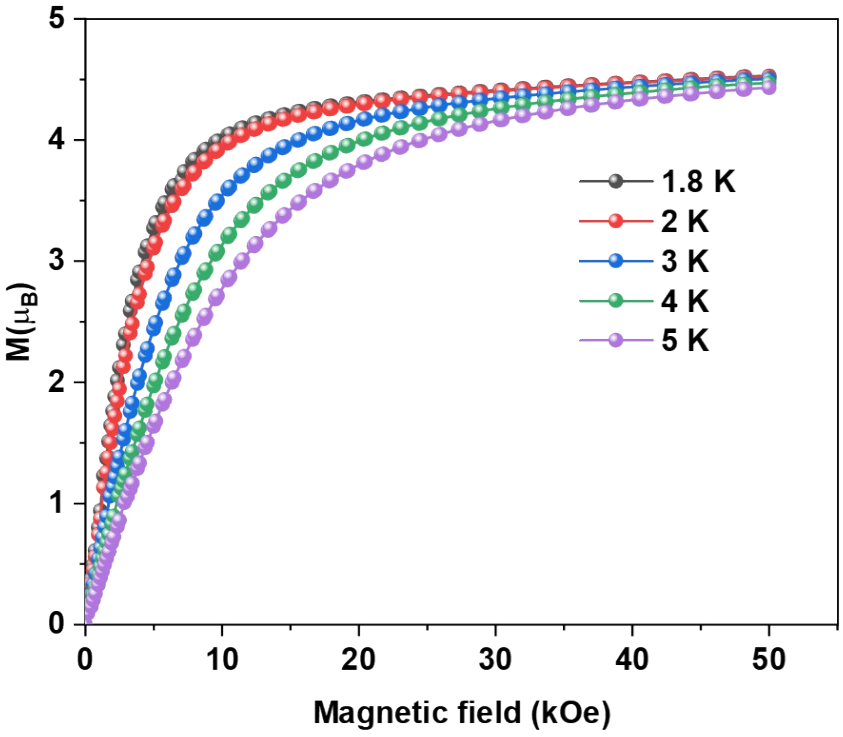

Figure S 7. Temperature-dependent field (*H*) versus moment (*M*) studies of compound **1**. The lines are guide to the eyes.

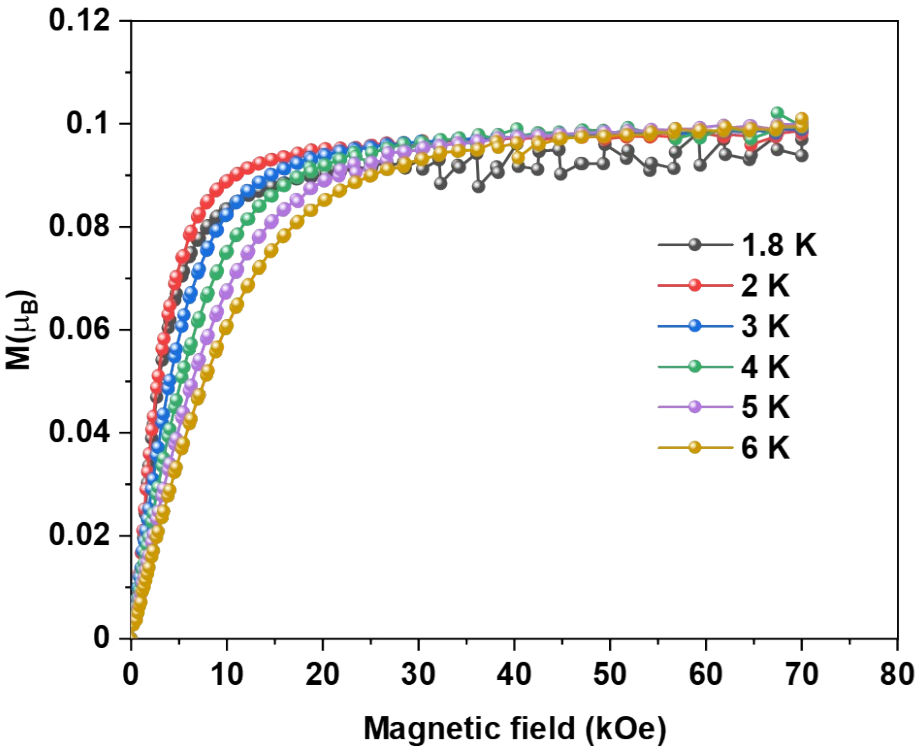

Figure S 8. Temperature-dependent field (*H*) versus moment (*M*) studies of compound **1@Y**. The lines are guide to the eyes.

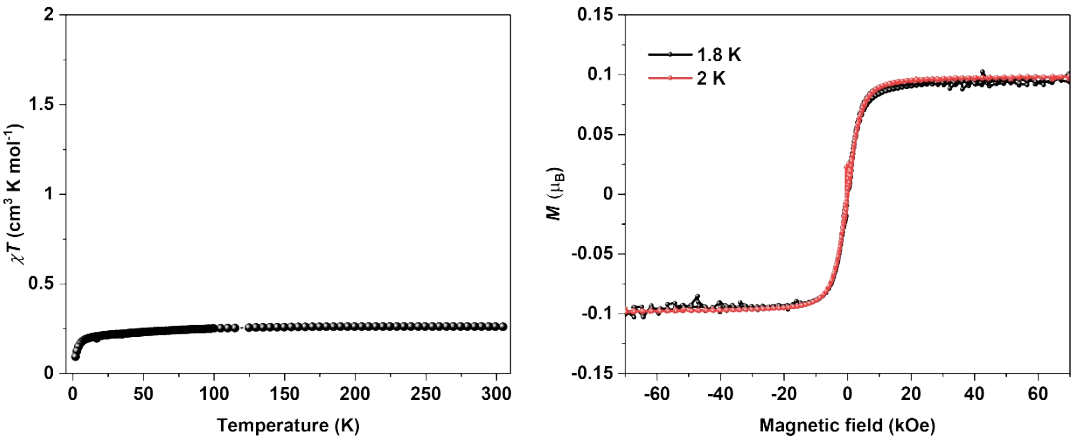

Figure S 9. (a) χT versus T and (b) field versus magnetization studies of **1@Y** compound at 1.8 K. The presence of magnetic hysteresis indicates that the Dy(III) compound is an SMM.

S4.2. Dynamic magnetic properties of compound 1

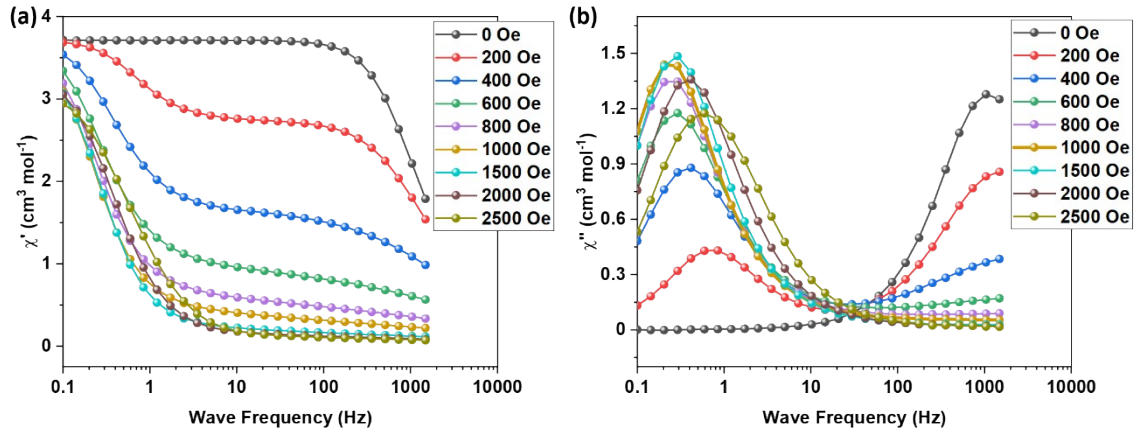

Figure S 10. DC field dependence of relaxation times. Applied DC field-dependent (a) in phase (χ') and (b) out-of-phase (χ'') susceptibilities of compound **1** at 3 K.

Table S5. DC Field (H_{DC}) versus lifetime (τ) of the stoichiometric compound.

H_{DC} (Oe)	τ (s)
0	1.61338E-4
200	1.51976E-4
400	0.58088
600	0.60774
800	0.66591
1000	0.67656
1500	0.56299

2000	0.39446
2500	0.258

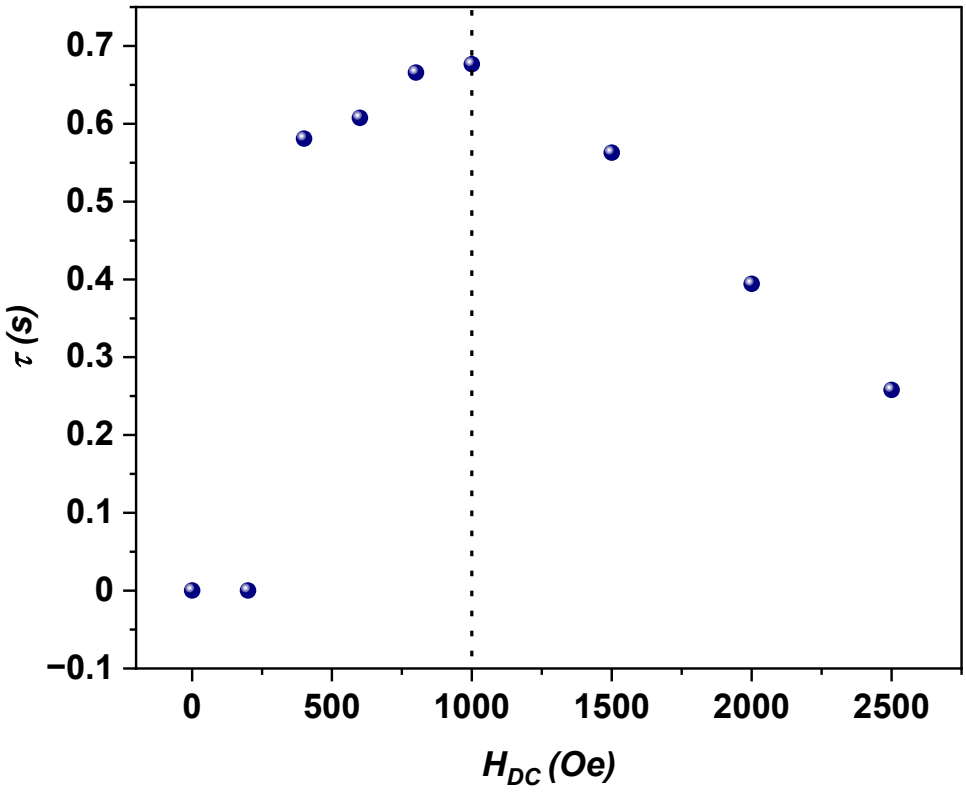

Figure S 11. Field versus relaxation time plot of compound **1**. The black dotted line shows the DC field (1000 Oe) at which the spin-relaxation is the slowest relative to other fields.

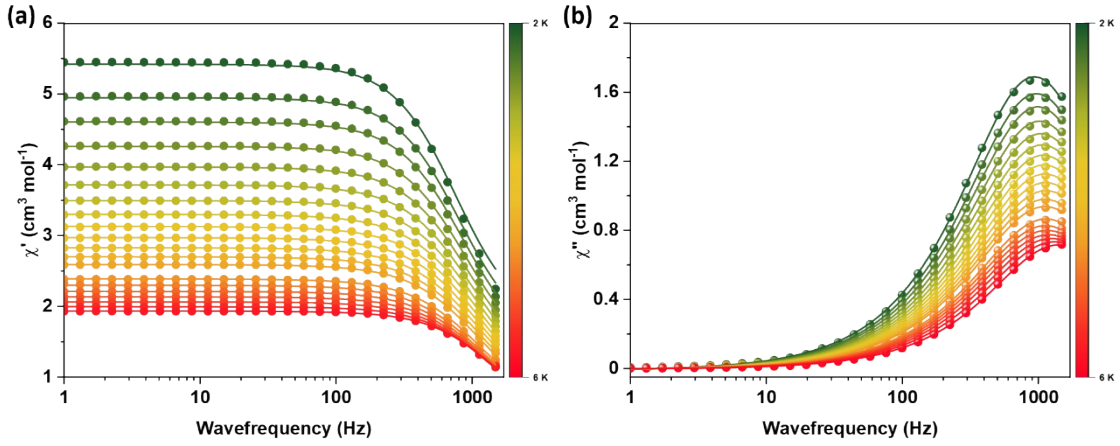

Figure S 12. Single-molecule magnet characteristics compound 1 at H_{DC} = 0 Oe. AC frequency-dependent (a) in phase (χ') and (b) out-of-phase (χ'') susceptibilities of the compound. The lines are the fits obtained by fitting the data employing the generalized Debye model.

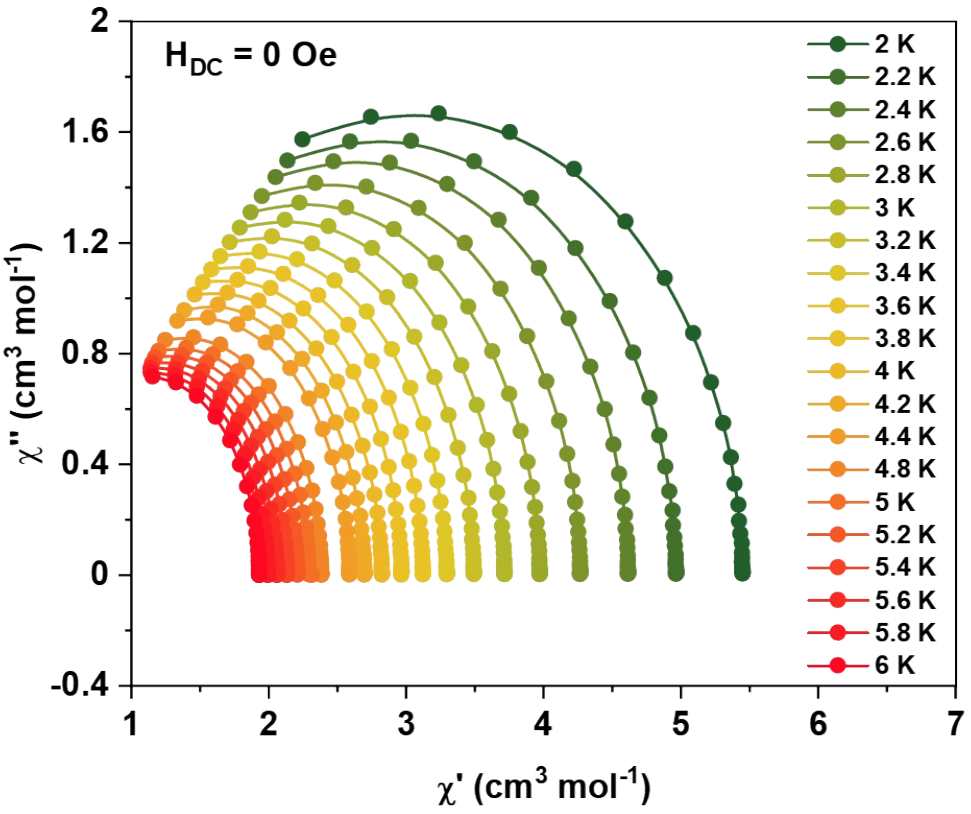

Figure S 13. Cole-Cole plots of compound **1** at H_{DC} = 0 Oe. The solid lines are guide to the eyes.

Table S6. Fitted parameters of compound **1** at H_{DC} = 0 Oe.

Temperature (K)	χ_T (cm^3mol^{-1})	χ_s (cm^3mol^{-1})	τ (s)	α
2	5.42	1.71	0.00021	0.0247
2.2	4.95	1.48	0.00019	0.031
2.4	4.60	1.32	0.000187	0.036
2.6	4.26	1.16	0.000178	0.04
2.8	3.96	1.02	0.000169	0.047
3	3.71	0.89	0.00016	0.054
3.2	3.49	0.79	0.000155	0.058
3.4	3.29	0.70	0.000150	0.06
3.6	3.12	0.63	0.000145	0.066
3.8	2.97	0.57	0.000142	0.06
4	2.83	0.53	0.000139	0.07
4.2	2.70	0.52	0.000141	0.067
4.4	2.59	0.52	0.000142	0.063
4.8	2.38	0.48	0.000139	0.062
5	2.29	0.48	0.00014	0.059
5.2	2.21	0.46	0.000137	0.056
5.4	2.13	0.44	0.000132	0.056
5.6	2.06	0.42	0.000127	0.053
5.8	1.99	0.40	0.000119	0.050
6	1.93	0.38	0.00011	0.047

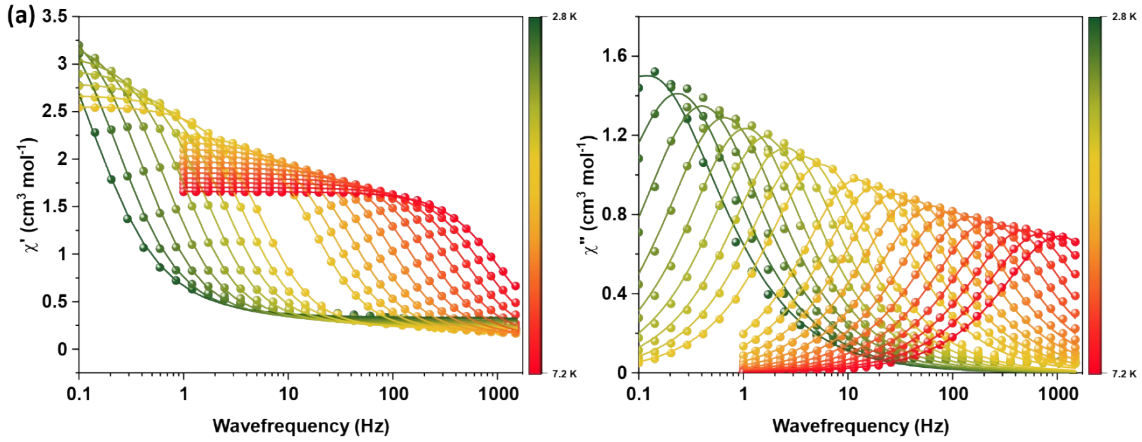

Figure S 14. Single-molecule magnet characteristic compound 1 at H_{DC} = 1000 Oe. AC frequency-dependent (a) in phase (χ') and (b) out-of-phase (χ'') susceptibilities of the compound. The lines are the fits obtained by fitting the data employing the generalized Debye model.

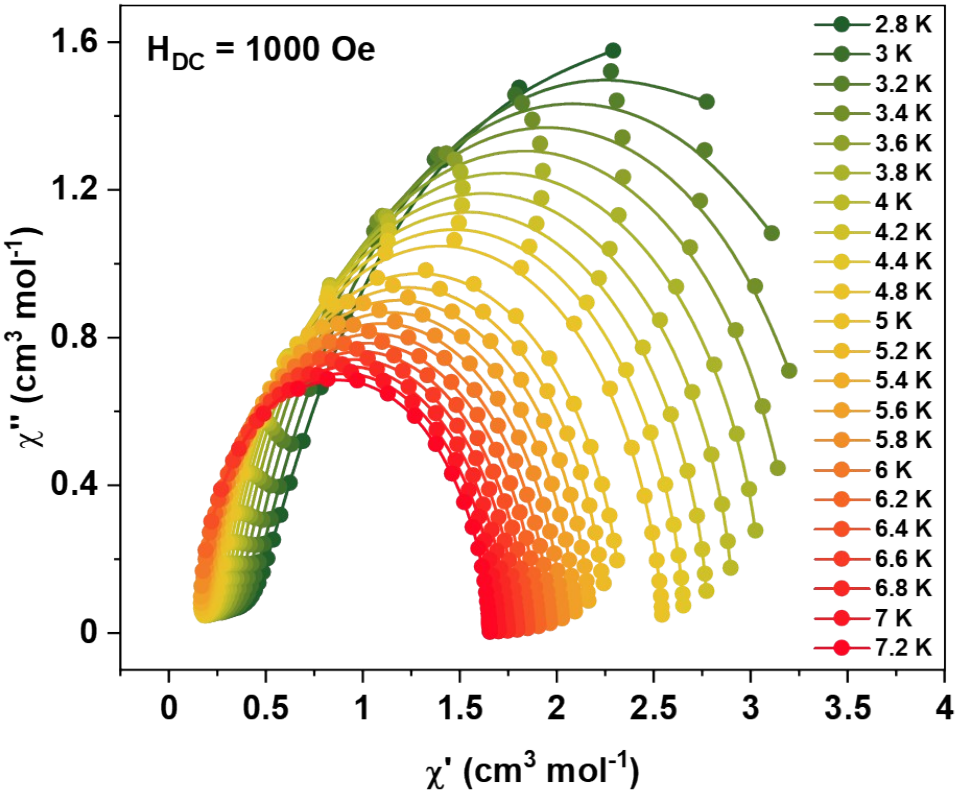

Figure S 15. Cole-Cole plots of compound **1** at H_{DC} = 1000 Oe. The solid lines are guide to the eyes.

Table S7. Fitted parameters of compound **1** at H_{DC} = 1000 Oe.

Temperature (K)	χ_T (cm^3mol^{-1})	χ_s (cm^3mol^{-1})	τ (s)	α
2.8	5.68	0.34	2.96	0.27
3	4.466	0.33	1.26	0.19
3.2	3.89	0.31	0.67	0.14
3.4	3.55	0.30	0.39	0.109
3.6	3.31	0.28	0.24	0.09
3.8	3.11	0.268	0.15	0.08
4	2.95	0.25	0.098	0.07
4.2	2.80	0.24	0.064	0.07
4.4	2.67	0.22	0.043	0.067
4.8	2.55	0.214	0.029	0.065
5	2.36	0.19	0.0131	0.065
5.2	2.26	0.18	0.0087	0.065
5.4	2.184	0.174	0.00577	0.066
5.6	2.107	0.164	0.0038	0.068
5.8	2.037	0.154	0.0025	0.07059
6	1.972	0.144	0.0016	0.073
6.2	1.91	0.132	0.00109	0.076
6.4	1.85	0.121	0.00072	0.079
6.6	1.80	0.109	0.00048	0.08528
6.8	1.75	0.093	0.000325	0.0872
7	1.70	0.079	0.00022	0.089
7.2	1.65	0.059	0.00015	0.093

S4.3. Dynamic magnetic properties of the **1@Y** compound

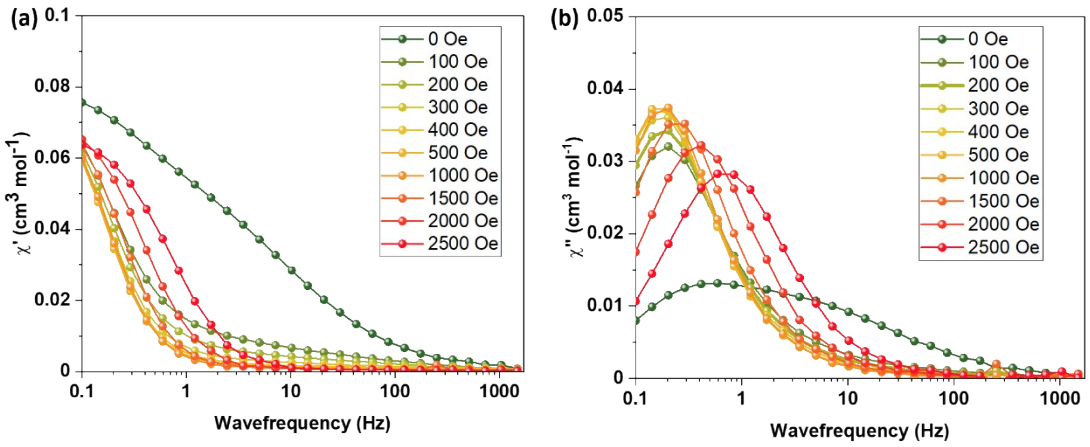

Figure S 16. DC field dependence of relaxation times. Applied DC field-dependent (a) in phase (χ') and (b) out-of-phase (χ'') susceptibilities of **1@Y**. The data have been collected at 3 K.

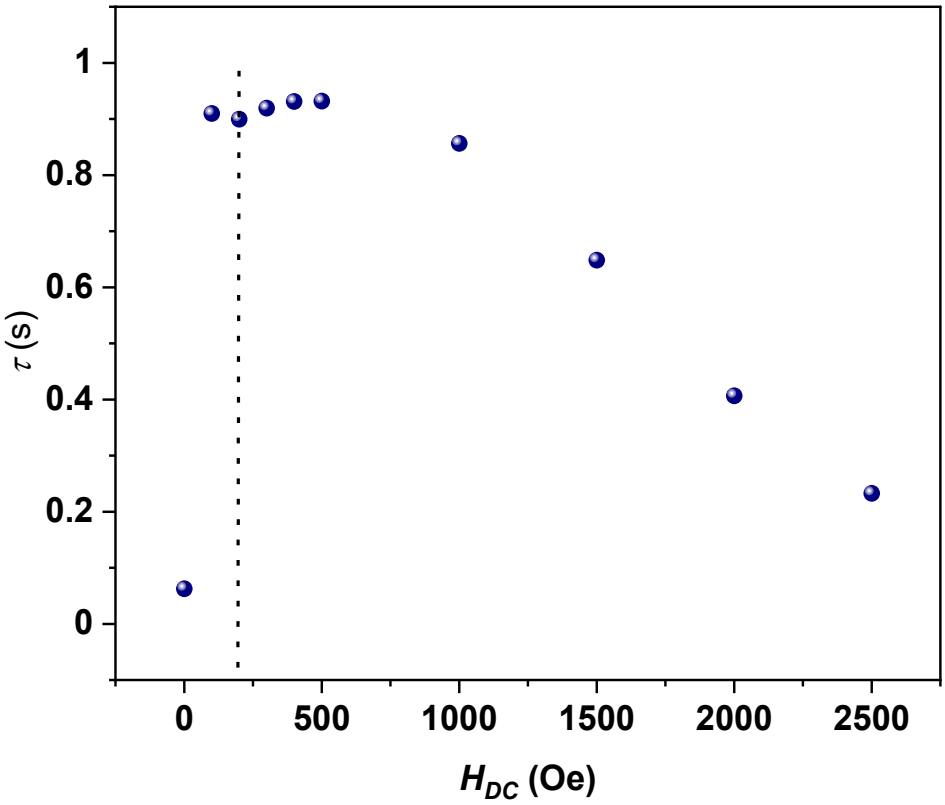

Figure S 17. Field versus relaxation time (τ) plot of **1@Y**. The black dotted line shows the field (200 Oe) at which the AC data was collected.

Table S8. Field versus lifetime data of the diluted compound.

H_{DC} (Oe)	τ (s)
0	0.06274
100	0.9099
200	0.8998
300	0.91922
400	0.9313
500	0.93189
1000	0.85656
1500	0.64853
2000	0.40654
2500	0.2329

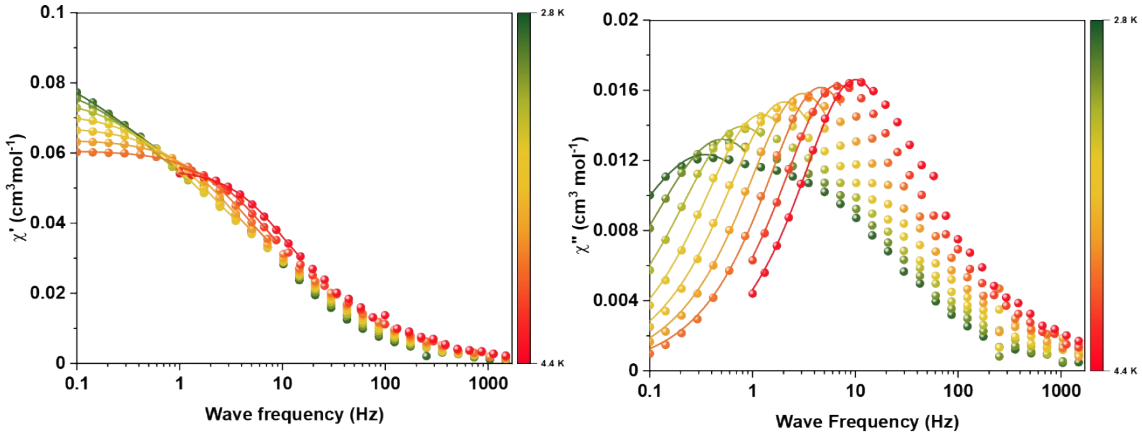

Figure S 18. SMM characteristics of **1@Y** at zero applied DC magnetic field. The data is shown in the 2.8 K-to-4.4 K temperature range. The lines are the fits obtained by fitting the data employing the generalized Debye model.

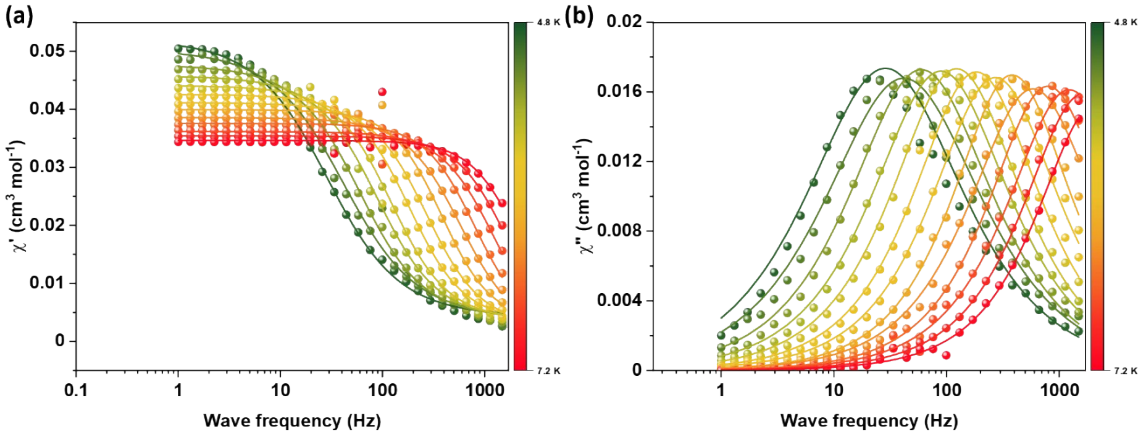

Figure S 19. Single-molecule magnet characteristic 1@Y at H_{DC} = 0 Oe. AC frequency-dependent (a) in (χ') and (b) out-of-phase (χ”) susceptibilities of **1@Y**. The data is shown in the temperature range 4.8 K-to7.2 K. The lines are the fits obtained by fitting the data employing the generalized Debye model.

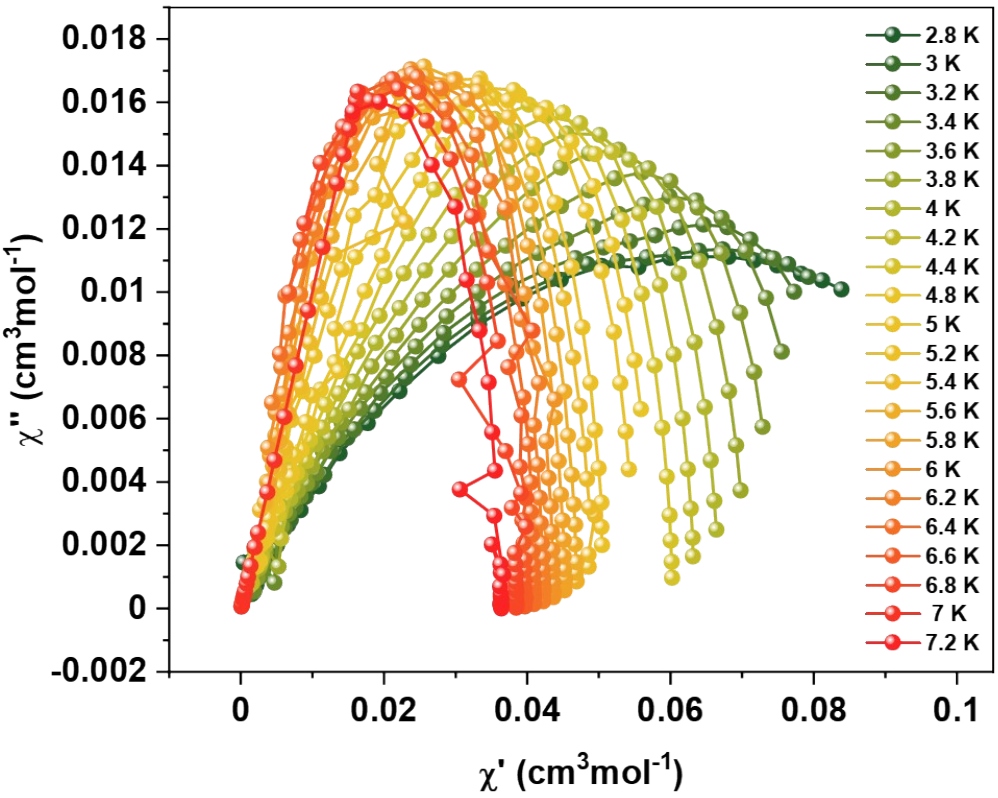

Figure S 20. Cole-Cole plots of **1@Y** in the absence of applied DC magnetic field.

Table S9. Fitted parameters of **1@Y** in the absence of applied DC magnetic field.

Temperature (K)	χ_T (cm^3mol^{-1})	χ_s (cm^3mol^{-1})	τ (s)	α
2.8	0.0878	0.0449	0.4629	0.3355
3	0.08149	0.0417	0.3147	0.2542
3.2	0.076	0.03761	0.2000	0.2006
3.4	0.07136	0.03376	0.1296	0.1589
3.6	0.06747	0.0283	0.0778	0.1542
3.8	0.06387	0.02502	0.0151	0.1301
4	0.06068	0.02203	0.0347	0.1136
4.2	0.05829	0.01903	0.0235	0.1171
4.4	0.05564	0.01647	0.0158	0.1048
4.8	0.0522	0.00413	0.0055	0.2030
5	0.05044	0.00385	0.0038	0.2050
5.2	0.047771	0.00387	0.00266	0.1503
5.4	0.0458	0.00357	0.00179	0.13004
5.6	0.04411	0.00357	0.0013	0.09942
5.8	0.04259	0.00348	0.0086	0.08357
6	0.04117	0.00262	0.00058	0.08655
6.2	0.03993	0.00337	0.00041	0.04727
6.4	0.03858	0.00124	0.00027	0.09137
6.6	0.03757	0.00232	0.00020	0.04872
6.8	0.03618	0.0028	0.00012	0.07331
7	0.03542	0.00077	0.00097	0.05516
7.2	0.03462	0.000209	0.00007	0.03949

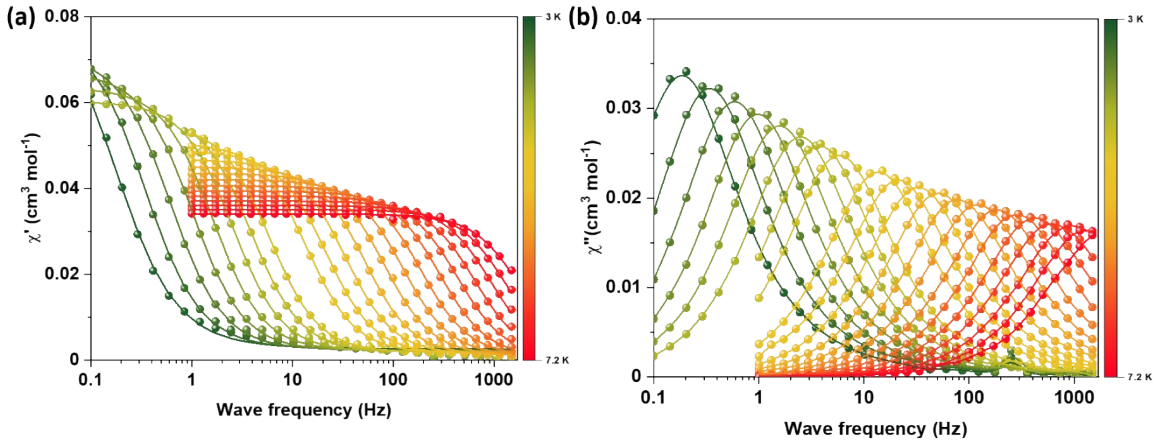

Figure S 21. Single-molecule magnet characteristic of **1@Y** at H_{DC} = 200 Oe. AC frequency-dependent (a) in (χ') and (b) out-of-phase (χ'') susceptibilities of the compound. The lines are the fits obtained by fitting the data employing the generalized Debye model.

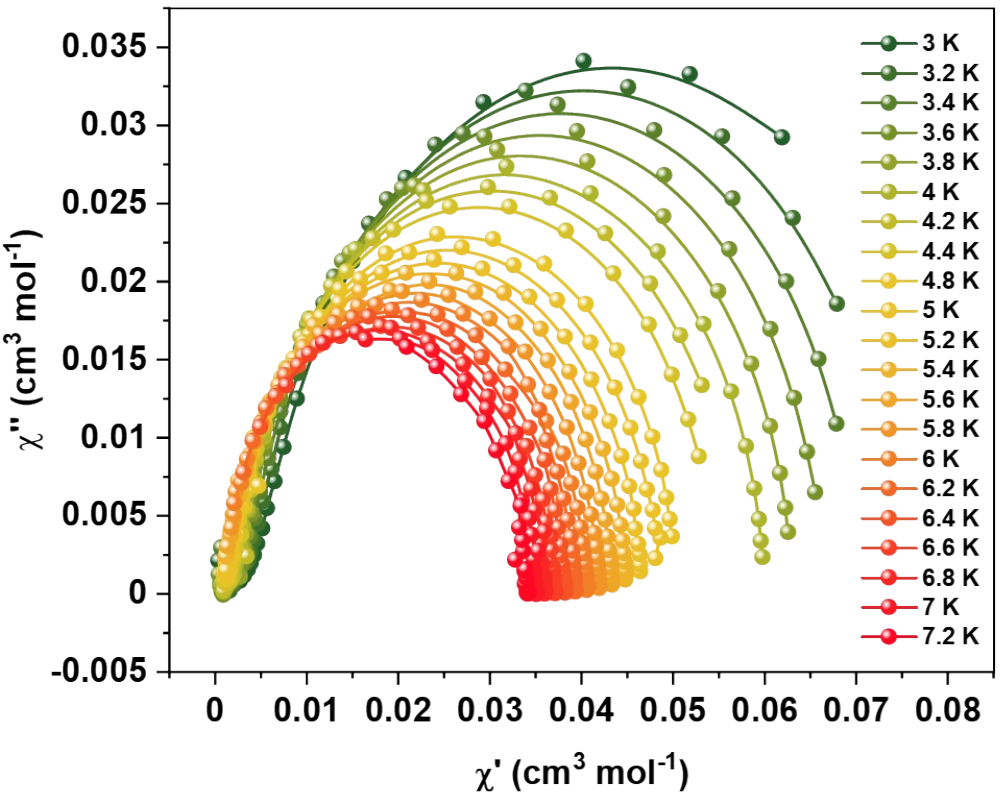

Figure S 22. Cole-Cole plots of **1@Y** at H_{DC} = 200 Oe. The solid lines are guide to the eyes.

Table S10. Fitted parameters obtained from the AC studies of **1@Y** at H_{DC} = 200 Oe.

Temperature (K)	χ_T (cm^3mol^{-1})	χ_s (cm^3mol^{-1})	τ (s)	α
3	0.08585	0.00256	0.8974	0.1324
3.2	0.07697	0.00246	0.45983	0.09107

3.4	0.07159	0.00224	0.26153	0.07313
3.6	0.06722	0.0021	0.15738	0.06055
3.8	0.06351	0.0021	0.098	0.05148
4	0.0603	0.00188	0.06246	0.04759
4.2	0.05805	0.00183	0.04121	0.051
4.4	0.05519	0.00169	0.02679	0.04591
4.8	0.05064	0.00161	0.01145	0.04228
5	0.04874	0.00134	0.0074	0.0438
5.2	0.0467	0.00129	0.00474	0.04011
5.4	0.04499	0.00115	0.00306	0.0362
5.6	0.04348	0.00105	0.00196	0.03983
5.8	0.04204	0.00097	0.00128	0.03859
6	0.04064	0.000915	0.00083	0.036
6.2	0.0394	0.00069	0.00055	0.036
6.4	0.03826	0.000361	0.000367	0.04319
6.6	0.03711	0.000132	0.000248	0.04498
6.8	0.03604	0.000244	0.000168	0.03827
7	0.03507	1.9594E-29	0.0001202	0.03836
7.2	0.03405	8.4313E-29	0.0000867	0.0384

S5. Photoluminescence studies of compound **1**

Excitation of an organic ligand coordinating to the Dy(III)-centre in the UV-region often induces $S_0 \rightarrow S_1$ transition, where S_0 and S_1 are ground and excited singlet states, respectively. The transition is followed by intersystem crossing (IC) to the triplet (T_1) state, promoted by the external heavy atom effect of the Dy(III) centre. Energy transfer from the triplet state (D; energy donor) to the $^4F_{9/2}$ receiving state (A; energy acceptor) followed by radiative deactivation of the later to ground ^6H_J states manifests as Dy(III)-centred luminescence in the visible and NIR regions.[4] In order for the above commonly observed pathway to be operative, a sizable energy gap ($\Delta E_{D\text{-}A}$) between the energy donor T_1 and acceptor $^4F_{9/2}$ states is imperative.[5] Unlike in the cases of Eu(III) and Tb(III) a definite $\Delta E_{D\text{-}A}$ value for Dy(III) compounds is yet to be established.[5] Remarkably, sensitization of the Dy(III)-centred luminescence via energy transfer from the S_1 state to the accepting Dy(III)-based levels has also been reported.[6]

For compound **1**, well-resolved characteristic Dy(III)-based transitions are observed at 2.4 K on excitation of the ligand-based transition at 359 nm, as shown in Figure 7 of the main script. In the following, we present quantitative estimates of various photophysical parameters and a discussion on mechanistic factors causing emission quenching with temperature rise from 2.4 K.

S5.1. Photoluminescence lifetime (τ) studies of compound **1**

The $^4F_{9/2}$ lifetime (τ) of about 18.42 µs (T = 2.4 K) is estimated by monitoring the emission at 574 nm (Figure S23). At 77 K, lifetime of 10.74 µs is observed (Figure S24) indicating temperature-dependent evolution of the excited state. The decays at 2.4 K and 77 K can be satisfactorily fitted with a biexponential function, the long component is considered as the

lifetime of the $^4F_{9/2}$ state. The short component is attributed to hot transition associated with the excited J = ±7/2 CF level of the $^4F_{9/2}$ multiplet, as discussed below. The lifetime value observed for the compound is comparable with the ones reported for Dy(III) compounds.[5]

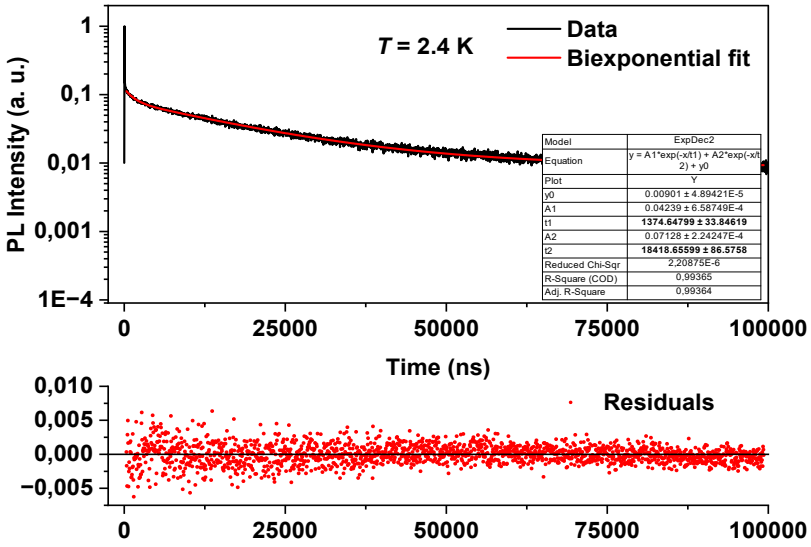

Figure S 23. PL decay of compound **1** at 2.4 K. The decay can be satisfactorily fitted with a biexponential function yielding lifetimes of 18.42 µs and 1.38 µs.

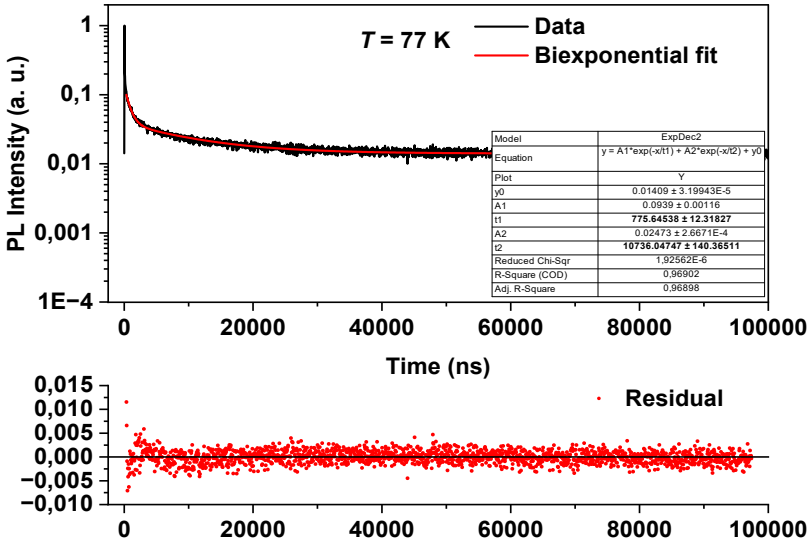

Figure S 24. PL decay of compound **1** at 77 K. The decay can be satisfactorily fitted with a biexponential function yielding lifetimes of 10.74 µs and 0.78 µs.

S5.1.1. Analysis of the biexponential decay of compound 1

The lifetime profiles of compound **1** at 2.4 K and 77 K are fitted using a biexponential function, see inset tables in Figures S23 and S24. From the lifetimes (τ1 and τ2) and the corresponding amplitudes (A1 and A2) obtained from the fitting results, the intensity weighed contribution of each component to the overall emission can be calculated using equation S1,

$$I(Ai, \tau i) = Ai \times \tau i / (A1 \times \tau 1 + A2 \times \tau 2) \qquad \text{Eq. S1}$$

where i is the component of interest $A1 \times \tau 1 \; or \; A2 \times \tau 2$.

By using the parameters obtained from the fits shown in Figures 23 and 24, we estimate intensity weighed contributions of 4.14% and 95.86% for the fast and slow components, respectively, at 2.4 K. At 77 K the contributions are 21.52% (fast) and 78.48% (slow). From the PL spectra shown in Figure 27 we estimate the energies of the J = ±9/2 (ex.0) and J = ±7/2 (ex.1) levels of the $^4F_{9/2}$ multiplet as 20994.73 cm^{-1} and 21025.19 cm^{-1}, respectively. Note, the assignments J = ±9/2 (ex.0) and J = ±7/2 (ex.1) are for the sake of discussion. Form the values we estimate the energy separation between the levels as 30.46 cm^{-1}. This value indicates that the J = ±7/2 (ex.1) level can be populated at sufficiently high temperatures such as 77 K. This results in the observation substantial intensity weighed component 21.52% (fast) corresponding to the hot band.

S5.2. Branching ratios and oscillator strengths of compound **1** at 2.4 K

An intense hypersensitive electric-dipole (ED)-induced $^4F_{9/2}\rightarrow{}^6H_{13/2}$ transition relative to the magnetic-dipole (MD)-induced $^4F_{9/2}\rightarrow{}^6H_{15/2}$ transition (which is not sensitive to the environment) is observed at 2.4 K. An asymmetric ratio of 6.2 is obtained from the integrated intensities of the $^4F_{9/2}\rightarrow{}^6H_{15/2}$ and $^4F_{9/2}\rightarrow{}^6H_{15/2}$ transitions (Table S11). These facets indicate that the Dy(III) centre is placed in a distorted LF environment.[7]

Table S11. Experimental variables used in the calculation of oscillator strengths ( ) for **1**.

Transition	2.4 K			
	Intensity (wavelength range)	β_R *x 100*	τ (s)	ν (10^{14} Hz)
$^4F_{9/2}\rightarrow{}^6H_{15/2}$	1679377 (470 nm to 490 nm)	13.05%	0.00001842	6.23
$^4F_{9/2}\rightarrow{}^6H_{13/2}$	10258500 (571 nm to 593 nm)	79.72%	0.00001842	5.22
$^4F_{9/2}\rightarrow{}^6H_{11/2}$	560032 (659 nm to 675 nm)	4.35%	0.00001842	4.50
$^4F_{9/2}\rightarrow{}^6H_{9/2}$	370206 (749 nm to 755 nm)	2.88%	0.00001842	3.98

To quantify how the asymmetric LF reflects on the branching ratios (βR) and oscillator strengths ( ), we estimated the overall emission intensity ($\sum I_{ij}$) and the emission intensities associated with each emissive transition (I_{ij}) by integrating the spectrum obtained at 2.4 K, see Table S11 for details. The branching ratio reflects on the intensities of the $^4F_{9/2}\rightarrow{}^6H_J$ transitions and is a ratio between the intensity (I_{ij}) of a particular $^4F_{9/2}\rightarrow{}^6H_J$ transition and total intensity ($\sum I_{ij}$) involving all the $^4F_{9/2}\rightarrow{}^6H_J$ transitions, as shown in Equation S2.

$$\beta R = \frac{Iij}{\sum Iij} \qquad \text{Eq. S2}$$

The calculation of oscillator strengths ( ) shed light on the transition probabilities of each $^4F_{9/2}\rightarrow{}^6H_J$ transition. The values of associated with the $^4F_{9/2}\rightarrow{}^6L_J$ transitions of **1** are obtained using Equation S3[8] and the values are collected in Table S12.

$$f = \frac{\varepsilon mc^3 \beta R}{2\pi n^2 e^2 v^2 \tau} \qquad \text{Eq. S3}$$

Where ε is vacuum permittivity, m is mass of electron, c is the speed of light, β_R is branching ratio, n is refractive index, e is electronic charge, v is frequency, and τ is lifetime. For calculating the oscillator strength, we used n = 1.5, lifetime estimated for the $^4F_{9/2}\rightarrow{}^6H_{13/2}$ transition (18.42 µs), and branching ratios collected in Table 12.

Table S12. Branching ratios (β_R) and oscillator strengths ( ) obtained for **1** at 2.4 K.

Transition	2.4 K	
	β_R	
$^4F_{9/2}\rightarrow{}^6H_{15/2}$	0.1305	1.09×10^{-5}
$^4F_{9/2}\rightarrow{}^6H_{13/2}$	0.7972	9.58×10^{-5}
$^4F_{9/2}\rightarrow{}^6H_{11/2}$	0.0435	6.98×10^{-6}
$^4F_{9/2}\rightarrow{}^6H_{19/2}$	0.02876	5.88×10^{-6}

S5.3. Temperature- and excitation-wavelength-dependent emission of compound 1

The emission process in **1** is temperature- and excitation-wavelength-dependent. At 300 K, the characteristic Dy(III)-based transitions are not observed. From temperature-dependent studies, we note a steady decrease of the Dy(III) centred emission intensity in the visible region (Figure S25-28) with increasing temperature upon excitation at 359 nm. At cryogenic temperatures, the excitation spectrum of the compound, measured by monitoring the emission at 574 nm (Figure S29-30), is composed of peaks with maxima centred around 263 nm and 359 nm. Additionally, discernible transitions of reasonable intensity spanning the 375 nm to 475 nm region are also observed. These peaks are assigned as f-f transitions involving Dy(III) as in Figure S29.[9] Crucially, the presence of Dy(III)-based f-f transitions in the excitation spectrum of the compound shows that Dy(III)-centred luminescence can also be obtained by directly addressing the f-f transitions. To check for the validity of the above point, the excitation wavelength dependence of the emission characteristics of the Dy(III) compound is studied at 2.4 K (Figure S31). When excited at 385 nm, 424 nm, 448 nm, and 469 nm, Dy(III)-based as well as a broad transition have been observed. On the other hand, excitation at 263 nm and 359 nm resulted in the observation of Dy(III) centred emission without the presence of the broad transition (Figure S31). To get insights into the temperature-dependent evolution of the emission process on direct f-f excitation, studies were performed by exciting the

compound at 424 nm (Figure S32). Remarkably, the Dy(III) emission is gradually weakened with a concomitant increase of the broad ligand-based transition upon temperature increase. Starting from around 70 K, a complete absence of Dy(III)-based emission is noted when the compound is excited at 424 nm. The broad transition is attributed to the ligand-based phosphorescence, considering the comparable nature of broad emission profiles observed for the Dy(III) and Gd(III) compounds (Figure S33). The observation of ligand-based phosphorescence upon excitation of Dy(III)-based f-f transition indicates energy migration from the Dy(III)-based levels to the triplet state of the ligand. Such observation coupled with the very weak Dy(III)-based $^4F_{9/2} \rightarrow {}^6H_J$ emission above 70 K upon excitation at 359 nm indicate back energy transfer (BET) from the $^4F_{9/2}$ state to the triplet state.

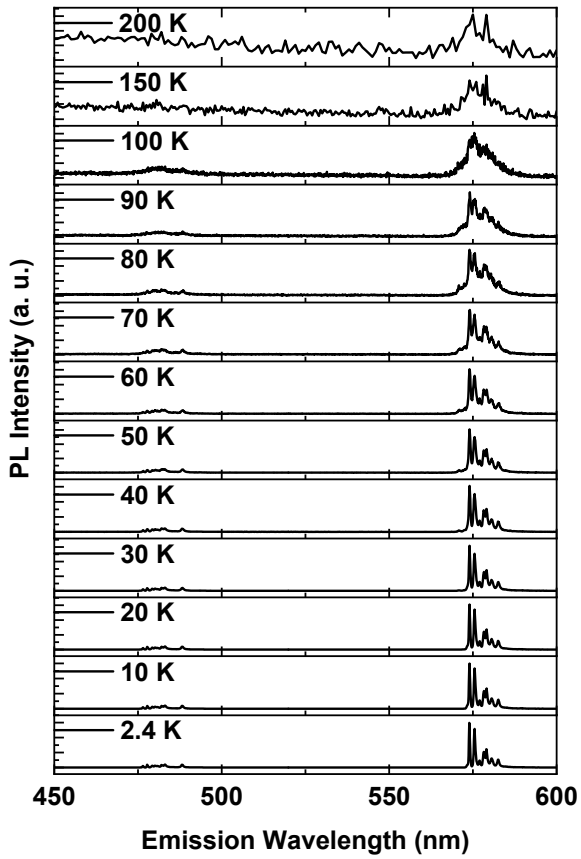

Figure S 25. Temperature-dependent PL characteristics of compound **1**. The spectra are obtained by exciting the sample at 359 nm.

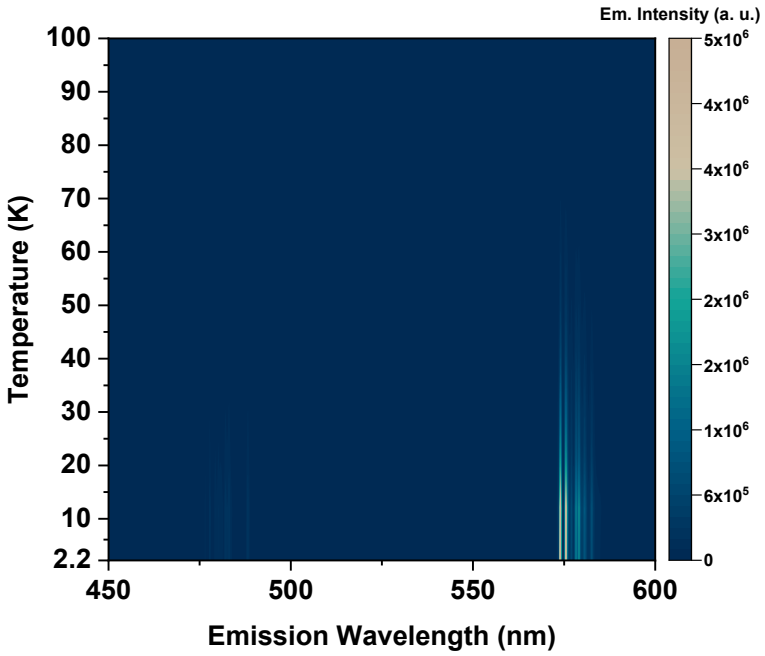

Figure S 26. Contour plot of temperature-dependent PL characteristics of compound **1**. The spectra are obtained by exciting the sample at 359 nm. The plot shows the gradual weakening of emission with increasing temperature. Above 70 K, the emission is almost quenched, especially the $^4F_{9/2} \rightarrow {}^6H_{15/2}$ transition.

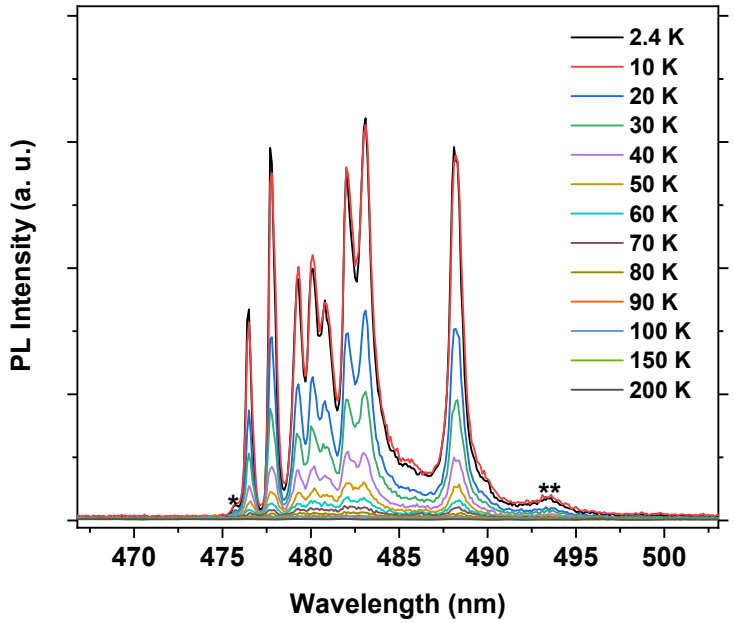

Figure S 27. Temperature-dependence of $^4F_{9/2} \rightarrow {}^6H_{15/2}$ transition of compound **1**. The spectra are obtained by exciting the sample at 359 nm. The small shoulder-like transition indicated by* is attributed to hot-band. The transition indicated by ** is tentatively attributed to vibronic transition.

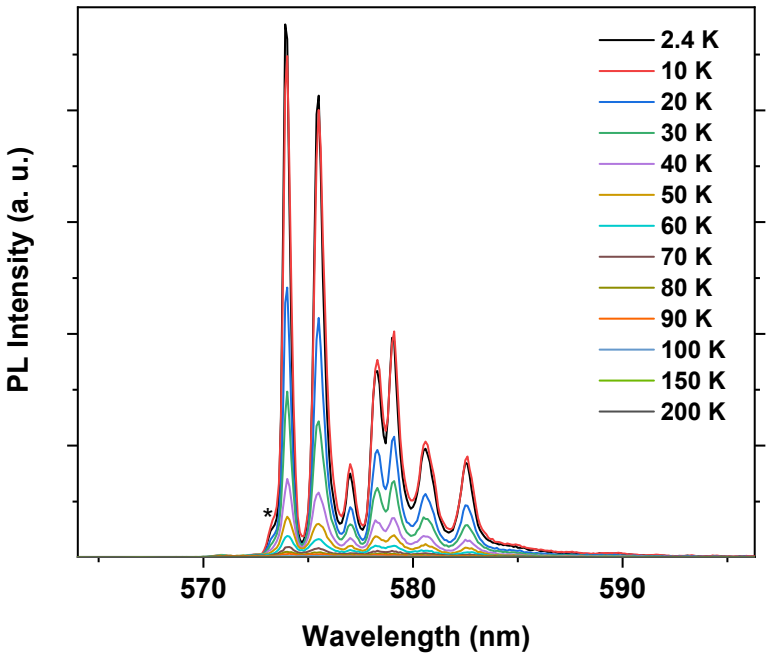

Figure S 28. Temperature-dependence of $^4F_{9/2} \rightarrow {}^6H_{13/2}$ transition of compound **1**. The spectra are obtained by exciting the sample at 359 nm.

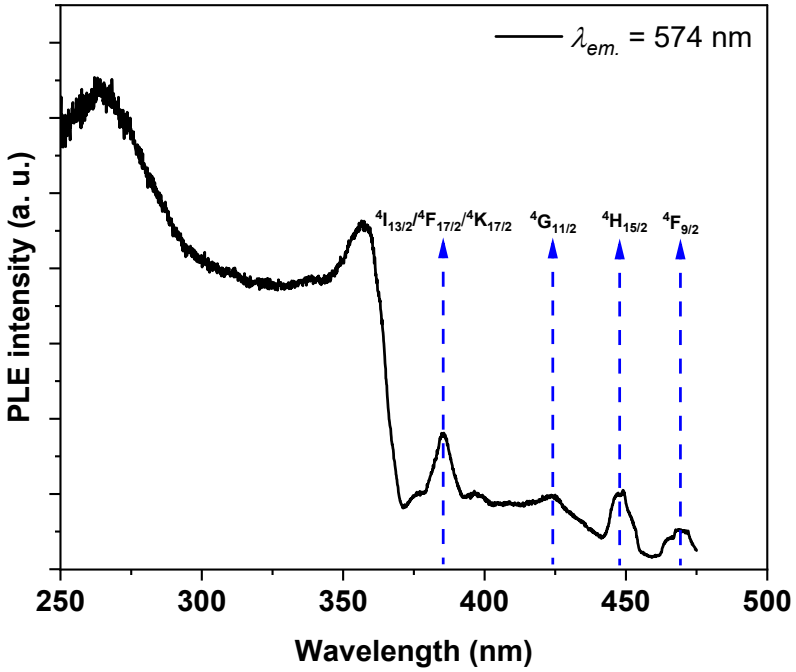

Figure S 29. Excitation spectra of compound **1** measure at 2.4 K by monitoring the emission at 574 nm. The transitions originate from the $^6H_{15/2}$ ground state multiplet.[9]

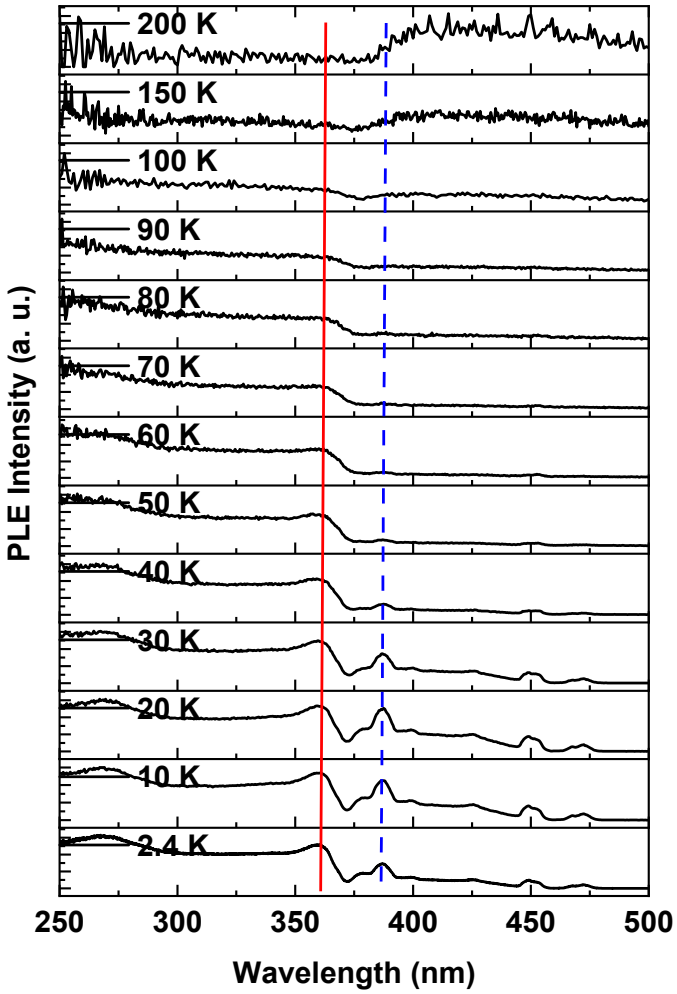

Figure S 30. Temperature-dependent excitation spectra of compound **1**. The emission was monitored at 574 nm. The red line indicates the temperature-dependent evolution of the ligand centred transition at about 359 nm. The blue dashed line indicates the temperature-dependent evolution of the Dy(III)-based $^{6}H_{15/2} \rightarrow {}^{4}I_{13/2}$ transition at about 385 nm.

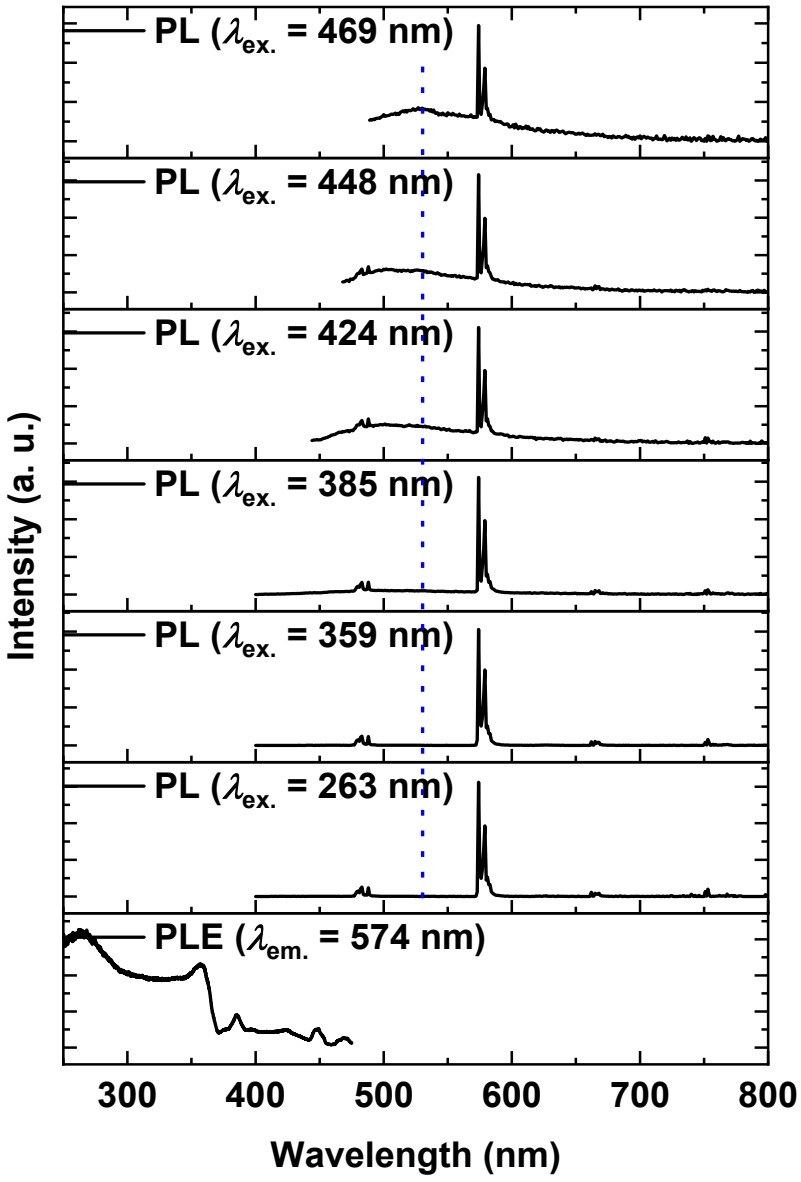

Figure S 31. Excitation wavelength-dependent emission characteristics of compound **1** at 2.4 K.

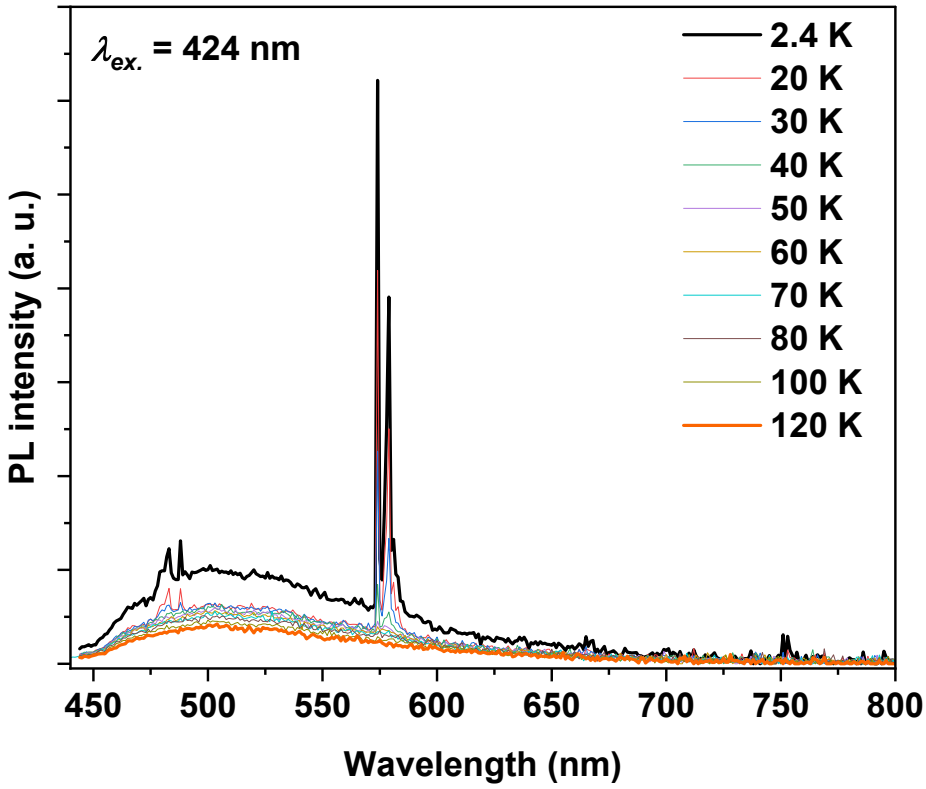

Figure S 32. Temperature-dependent emission characteristics of compound **1** upon exciting the compound at 424 nm.

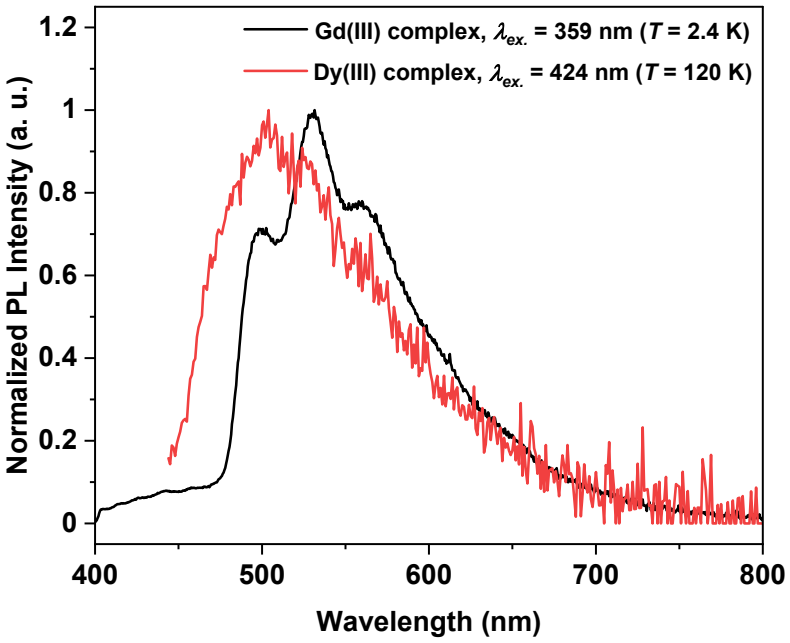

Figure S 33. Normalized emission spectra of compounds **1** (Dy(III)) and **3** (Gd(III)).

S5.4. Emission colour of compound 1

A yellow-green emission (commission internationale de l'éclairage (CIE) coordinates—x = 0.465 and y = 0.475) is observed for **1** at 2.4 K on excitation at 359 nm (Figures S34 and Table S13, entry F). Remarkably, the emission process in **1** is excitation wavelength-dependent at 2.4 K (Figure S34 and Table S13). Such dependency leads to the observation of myriads of colours (Table S13) at 2.4 K. The presence of ligand-based emission on excitation at 424 nm caused a change in the emission colour, as inferred from the CIE coordinates—x = 0.324 and y = 0.465—depicted in Figure S34 and Table S13, see entry J. Temperature-dependent emission colour variation of compound **1** at λex. = 359 nm (Figure S35 and Table S14) and λex. = 424 nm (Figure S36) is also presented in the following.

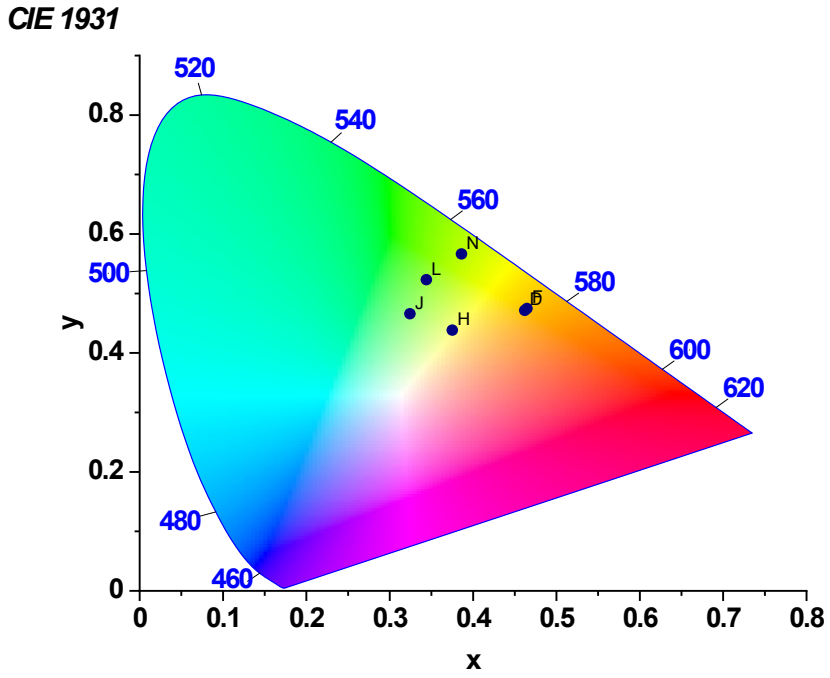

Figure S 34. Excitation wavelength-dependent CIE coordinates of compound **1** at 2.4 K.

Table S13. Excitation wavelength-dependent CIE coordinates of compound **1** at 2.4 K.

$\lambda_{ex.}$	CIE Coordinates	
	x	y
263 (D)	0.461	0.471
359 (F)	0.464	0.474
385 (H)	0.374	0.438
424 (J)	0.324	0.465
448 (L)	0.343	0.523
469 (N)	0.385	0.566

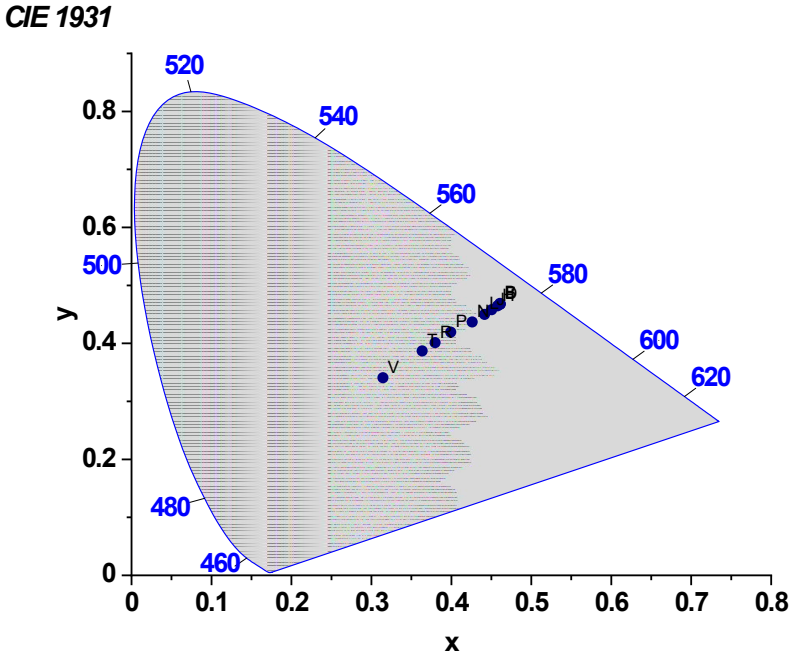

Figure S 35. Temperature-dependent CIE coordinates of compound **1** in the range of 2.4 K to 100 K, λex. = 359 nm.

Table S14. Temperature-dependent CIE coordinates of compound **1** at $\lambda_{ex.}$ = 359 nm.

T/K	CIE Coordinates	
	x	y
2.4 (D)	0.460	0.468
10 (F)	0.461	0.467
20 (H)	0.457	0.464
30 (J)	0.450	0.458
40 (L)	0.441	0.450
50 (N)	0.426	0.436
60 (P)	0.399	0.319
70 (R)	0.379	0.401
80 (T)	0.363	0.387
100 (V)	0.314	0.340

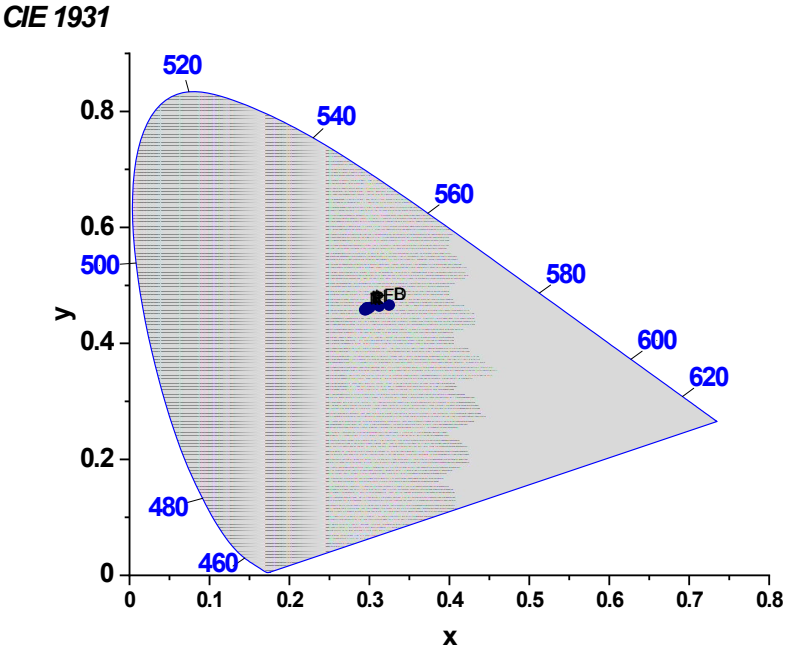

Figure S 36. Temperature-dependent CIE coordinates of compound **1** in the range of 2.4 K to 120 K, $\lambda_{ex.}$ = 424 nm. CIE coordinates: 2.4 K: x = 0.324; y = 0.465. 120 K: x = 0.295; y = 0.457. As the changes in the CIE coordinates are small, a table is not prepared, listing the values of the coordinates.

S5.5. Insights into temperature-mediated PL quenching of 1

The observation of well-resolved $^4F_{9/2} \rightarrow {}^6H_J$ emission of the Dy(III) compound (**1**) at cryogenic temperatures, emission intensity reduction with temperature increase, and complete absence of emission at RT merit explanation. The $^4F_{9/2}$ state is located at 21008 cm^{-1}, as estimated from the intersection point of the PLE and PL spectrum of the compound (Figure S37) comparable with the values reported for Dy(III) compounds.[4,6,10]

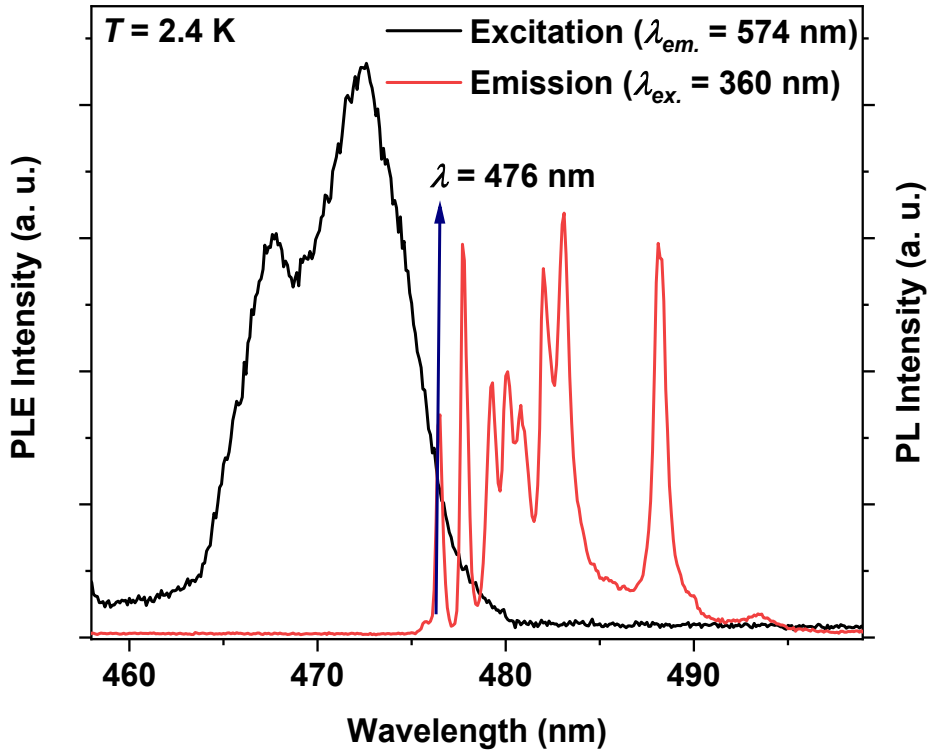

Figure S 37. Photoluminescence excitation (PLE) and emission spectra of compound **1** obtained at 2.4 K.

To find the nature of ligand-based electronic states involved in the energy transfer process to the Dy(III) centre, an estimate of triplet state energy (E_T) of the ligand is necessary. The E_T value of the ligand is estimated from the phosphorescence spectrum of the corresponding Gd(III) compound (**3**) at 2.4 K (Figures S38 and S39). The procedure is adopted considering the fact that the lowest excited state ($^6P_{7/2}$) of Gd(III) is located at a higher energy (about 32000 cm^{-1}) than the ligand centred triplet state.[9] For the ligand, E_T = 21186 cm^{-1} (472 nm) is estimated from the phosphorescence spectrum of Gd(III) compound by considering the intersection of the tangent line drawn at the onset of the high energy side of the phosphorescence spectrum (Figure S39). The observed lifetime of about 1.9 ms (Figure S40) confirms the ligand-based phosphorescent nature of the emission of the Gd(III) compound.

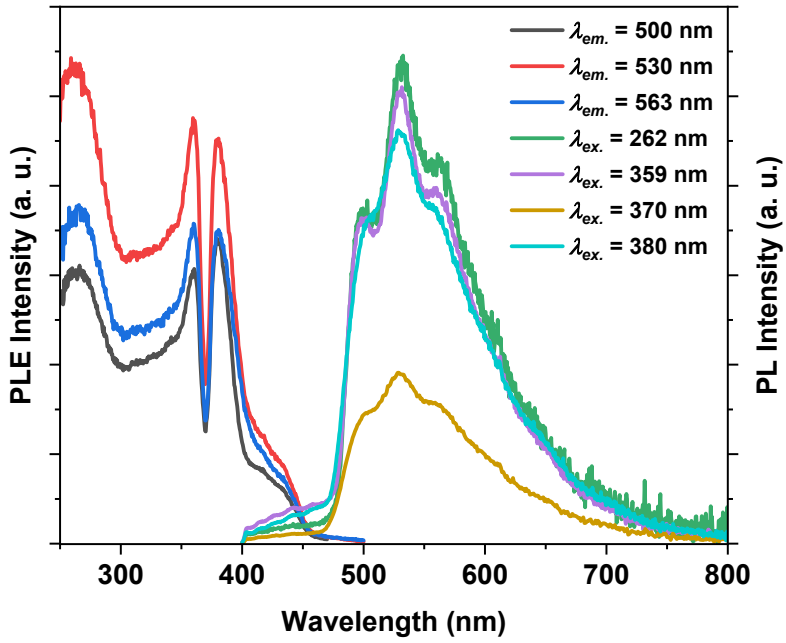

Figure S 38. Photoluminescent excitation and emission spectra of compound **3** at 2.4 K.

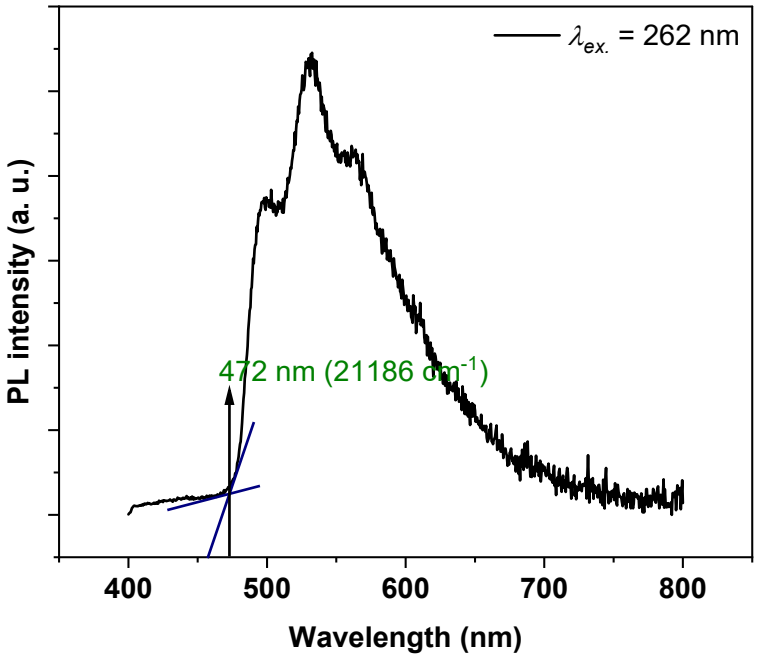

Figure S 39. Estimation of the triplet energy (E_T) of the ligand. Phosphorescence emission spectrum of compound **3** measured at 2.4 K ($\lambda_{ex.}$ = 262 nm). By considering the onset of emission edge (the intersection between the blue lines, 472 nm) E_T = 21186 cm^{-1} is estimated.

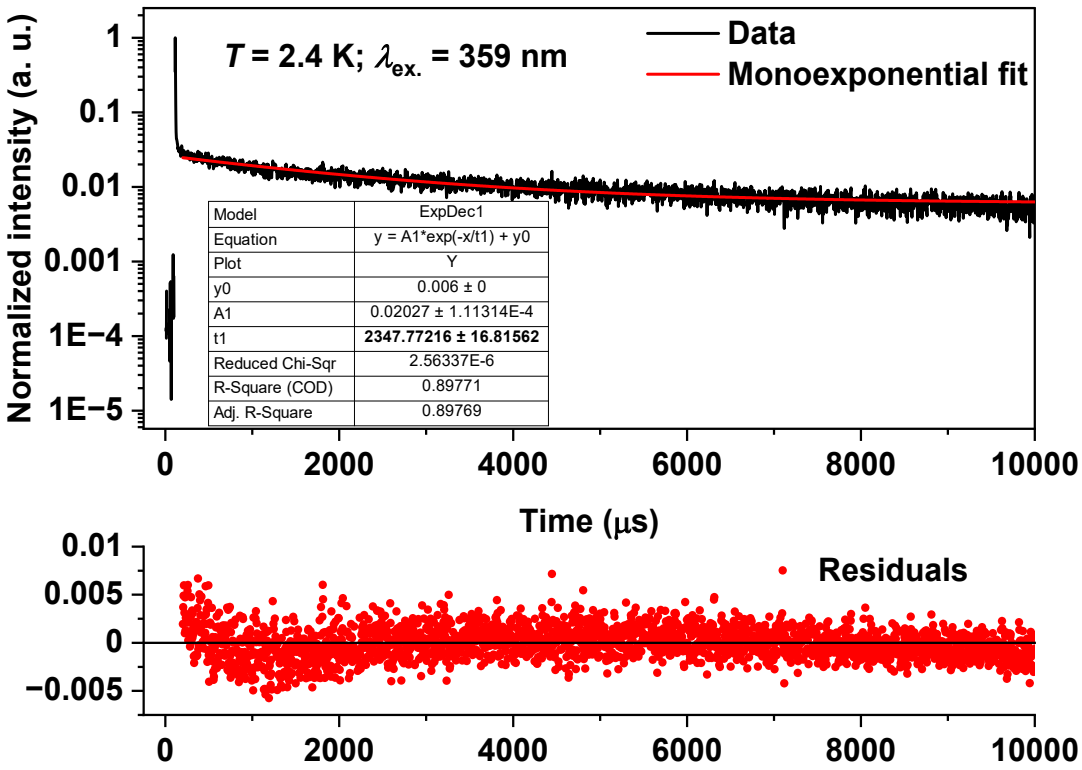

Figure S 40. Triplet lifetime of the ligand. Emission decay of compound **3** at 2.4 K. The decay can be satisfactorily fitted with a monoexponential function yielding the triplet lifetime of 1.89 ms. The sample was excited at 359 nm and the emission was monitored at 530 nm.

A comparison between the $^4F_{9/2}$ state energy of the Dy(III) centre (21008 cm^{-1}) and triplet energy of the ligand (21186 cm^{-1}) indicates that the ligand-based triplet state lies in close proximity to the Dy(III)-based $^4F_{9/2}$ state. By comparing the excitation spectra of the Gd(III) and Dy(III) compounds, the peaks centred at 263 nm and 359 nm are assigned to ligand-based transitions. A peak centred at 361 nm is observed in the excitation spectrum of the isostructural Eu(III) compound (Figure S41), matching with the position of the low-energy peak (359 nm) observed for the Dy(III) and Gd(III) compounds, confirming the above assignment. We assign 27855 cm^{-1} as the singlet state (S_1) energy of the ligand, considering the second highest energy maxima of 359 nm.

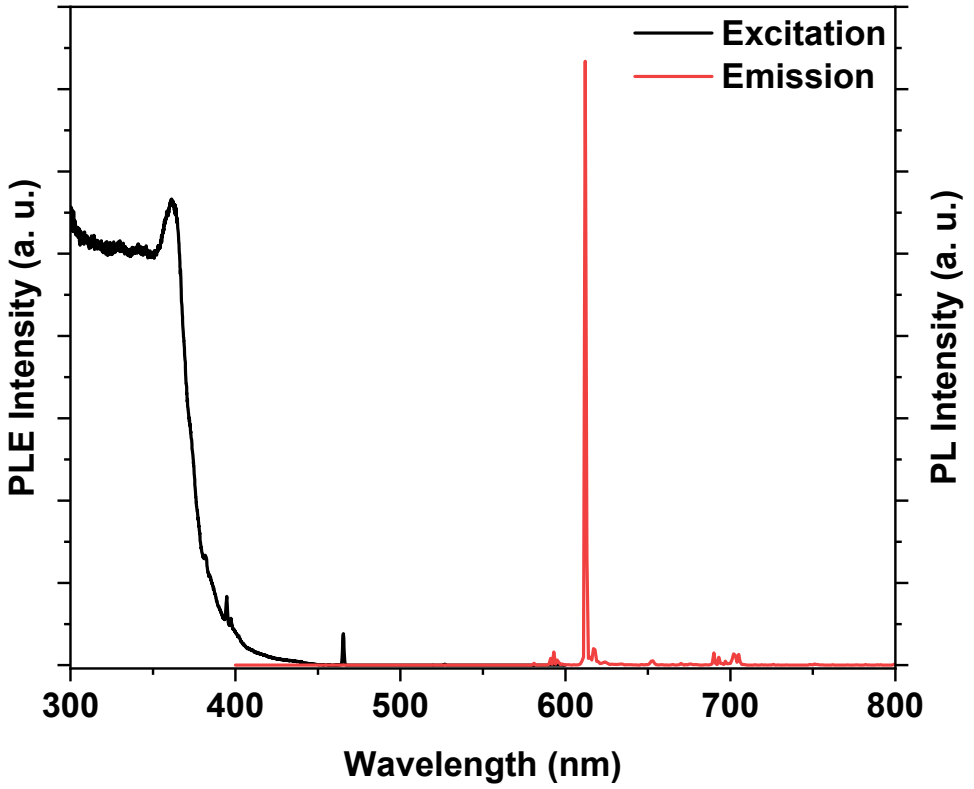

Figure S 41. Photoluminescence excitation and emission spectra of Eu(III) compound measured at 2.4 K.

A remarkable point here is the close energetic proximity of the $S_0 \rightarrow T_1$ (21186 cm^{-1}) and $^6H_{15/2} \rightarrow {}^4F_{9/2}$ (21008 cm^{-1}) transitions. And the energy difference between the ligand-based triplet and Dy(III)-based $^4F_{9/2}$ states is 178 cm^{-1}. At cryogenic temperatures, especially at 2.4 K, the energy difference is not bridged by back energy transfer (BET) from the $^4F_{9/2}$ state to the triplet-state. As a consequence, well-resolved Dy(III)-based emission is observed. Such emission is also facilitated by the long-lived triplet state, featuring τ = 1.891 ms. Overall, a sensitized pathway involving the triplet level of the ligand can be inferred at 2.4 K. Additionally, the absence of ligand-based phosphorescence, when the compound was excited at 359 nm, indicate efficient energy transfer from the triplet state to the receiving $^4F_{9/2}$ state.

The decreasing Dy(III)-based emission intensity with increasing temperature and its near absence above 70 K indicate the operation of deactivation pathways. To get a quantitative picture of the deactivation, we have fitted the temperature-dependent intensity variation of the $^4F_{9/2} \rightarrow {}^6H_{13/2}$ transition using Arrhenius-like Equation S4, where I_0, A, and E_a are the $^4F_{9/2} \rightarrow {}^6H_{13/2}$ intensity at 2.4 K, preexponential factor, and activation energy, respectively.

$$I(T) = I_0/1+A\cdot e^{-Ea/(k_B T)} \qquad \text{Eq. S4}$$

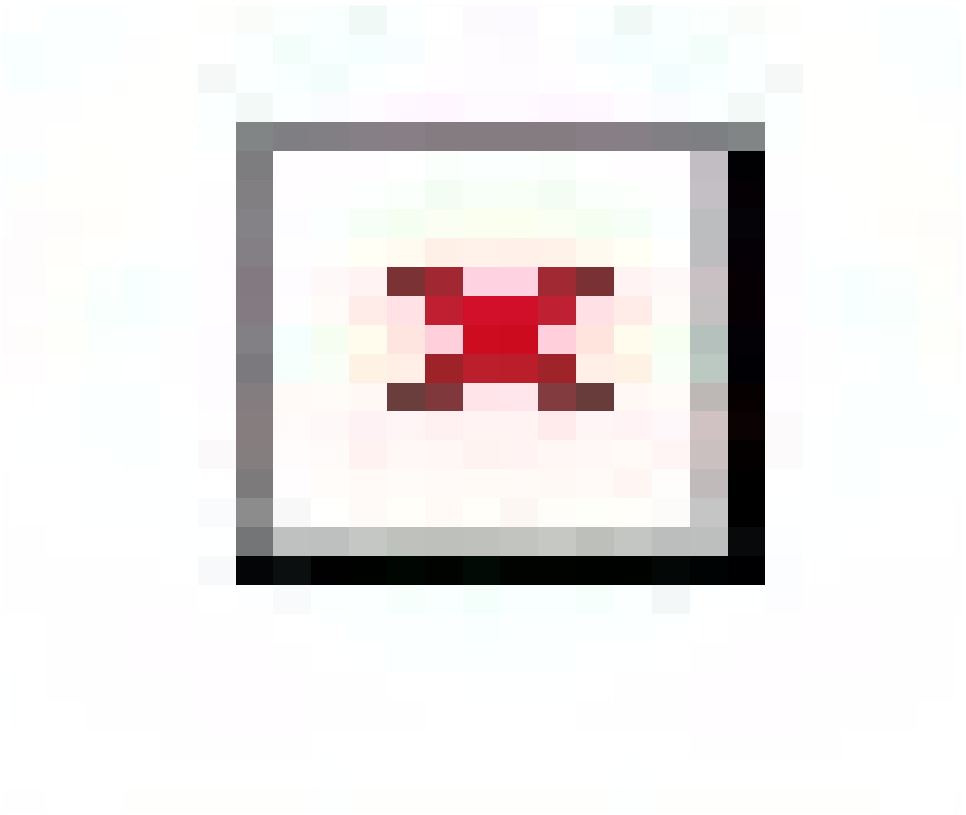

Figure S 42. Intensity (*I*) versus *T* plot of compound **1**. The intensity of the $^4F_{9/2} \rightarrow {}^6H_{13/2}$ transition is used.

From the fit (Figure S42), we estimate activation energy (E_a) of about 222 K (154.3 cm^{-1}) and preexponential factor of about 633. The estimated E_a value is comparable with the energy difference (178 cm^{-1}) between the triplet level of the ligand and Dy(III)-based $^4F_{9/2}$ level. The preexponential factor reflects on the frequency of thermally-induced deactivation attempts per unit time. Such attempts are governed by the temperature and density of vibrational states. The moderate value of 633 indicates not so dominant deactivation of the $^4F_{9/2}$ level. However, molecular vibrations increase concomitantly with temperature, and such increase could enhance the coupling between the close-lying triplet and $^4F_{9/2}$ levels, facilitating BET with temperature rise, in line with the observed intensity drop with temperature. The presence of curvature in the 20 K to 50 K region of the plot shown in Figure S42 indicates the involvement of multiphonon relaxation channels in emission quenching, presumably, promoted by vibronic coupling.

In a nutshell, we propose that both back energy transfer (BET)—from the $^4F_{9/2}$ to the triplet level of the ligand—and multiphonon relaxation processes contribute to the observed quenching behaviour. This underscores the importance of triplet-$^4F_{9/2}$ energy difference and vibrational dynamics in modulating temperature-dependent emission intensity of **1**. Studies on the temperature-dependent emission characteristics of the deuterated version of compound **1** would shed more light on the mechanistic aspects of the thermally-induced emission quenching, especially on vibrational contributions.

S6. Analysis of ligand-field symmetry around Dy(III) in compound **1**

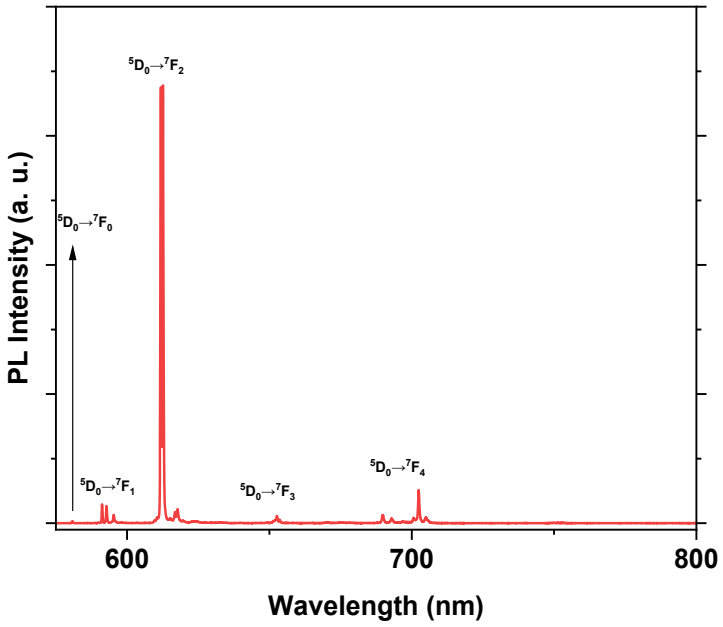

Figure S 43. Emission spectrum of previously studied Eu(III) compound—$[Eu(BA)_4](pip)$ (**2**). The data is collected at 2.4 K. The $^5D_0 \rightarrow ^7F_J$ (J = 0, 1, 2, 3, or 4) are labelled in the figure.

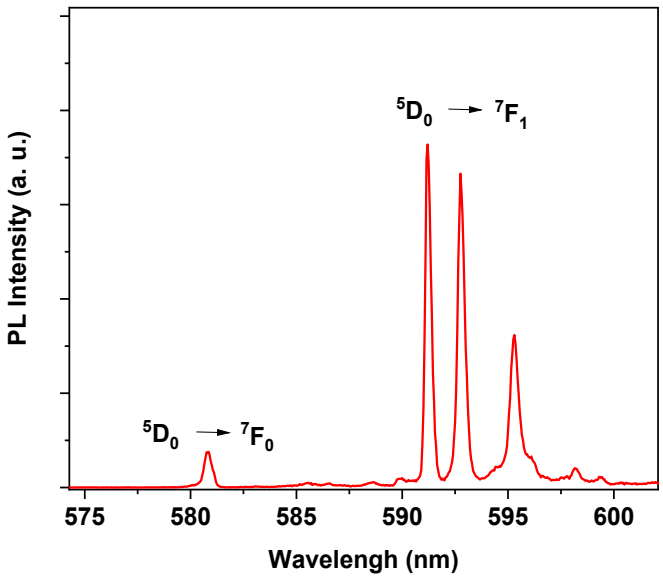

Figure S 44. The figure shows the $^5D_0 \rightarrow ^7F_0$ and $^5D_0 \rightarrow ^7F_1$ transitions of **2** in the 575 nm to 600 nm regime. The presence of single $^5D_0 \rightarrow ^7F_0$ transition indicates a single Eu(III) site. The observation of three well-resolved peaks of the $^5D_0 \rightarrow ^7F_1$ transition and $^5D_0 \rightarrow ^7F_0$ transition indicates the low-symmetry coordination environment around the Eu(III).

A correlation between magnetic and luminescence properties of Eu(III) compounds could be established by estimating the LF splitting from the studies. Comparable values obtained from

the studies serve as an additional support for the LF geometry assignment. Remarkably, such comparisons also provide insights into possible intermolecular magnetic interactions between the Ln(III) centres.[11–13] The magnitude of splitting between the $^7F_0$ and $^7F_1$ states can be estimated from DC magnetic studies (Figure 45) employing the relation: $(\chi_M)_{LT} = 2.086 \times 10^{-3}/\lambda$, where $(\chi_M)_{LT}$ is low-temperature molar magnetic susceptibility, λ is crystal field splitting.[14] For the Eu(III) compound, the χ_M gradually increases (Figure S45b) with temperature until 100 K. In the 100 K to 25 K temperature range, the χ_M remains stable. Below 25 K, the value again increases due to the presence of paramagnetic Ln(III) impurities. By using the χ_M value of 0.0586 $cm^3\ mol^{-1}$ at 50.2 K, λ = 355.67 cm^{-1} is estimated. To compare the λ estimated from the magnetic measurement with the one estimated from the low-temperature PL study, we have determined the relative energies of $^7F_1$ states by taking the $^7F_0$ energy as 0. From the PL data, we obtain, $E(^7F_0)$ at 17217.9273 cm^{-1} and $E(^7F_1)$ components (Figure S44) at 16915.6080 cm^{-1}, 16971.0880 cm^{-1} and 16798.3940 cm^{-1}. From the values, we deduce that the $^7F_1$ states are situated at 302.32 cm-^{1}, 346.84 cm^{-1}, and 419.93 cm^{-1} above the $^7F_0$ state. The average of the energies of the $^7F_1$ states is 356.36 cm^{-1}, in excellent agreement with the λ (355.67 cm^{-1}) obtained from the magnetic data. Importantly, the comparable values of λ obtained from the magnetic and PL measurements indicate the absence of intermolecular magnetic interactions[11] and lends credibility to the assignment of distorted SAP LF geometry in the Eu(III) compound by excluding contaminations from excited ^5D_J manifold and intermolecular magnetic interactions.

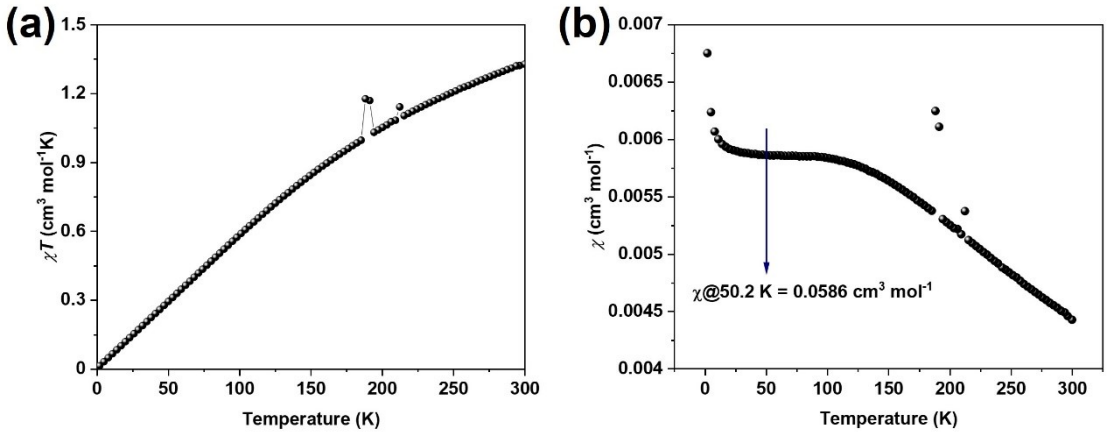

Figure S 45. (a) χT versus T and (b) χ versus T plots of Eu(III) compound **2**.

S7. CF splitting energies of transitions associated with compound **1**

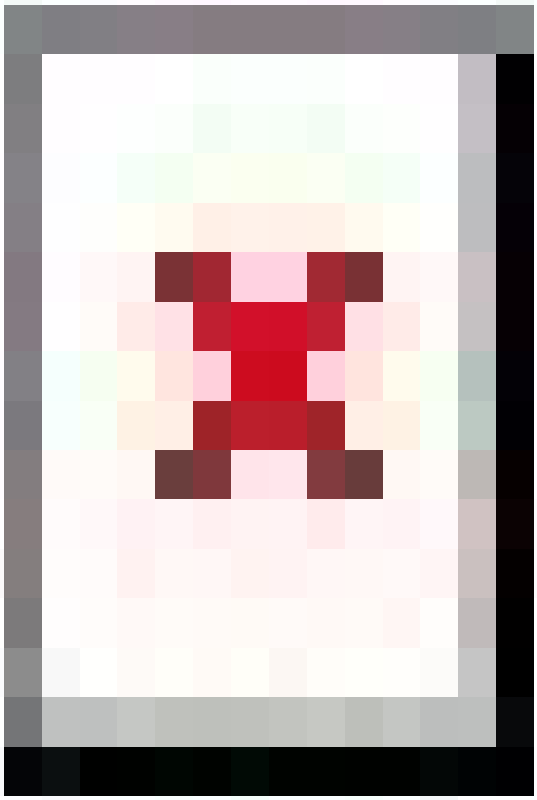

Figure S 46. Fitting parameters associated with the $^4F_{9/2} \rightarrow {}^6H_{15/2}$ transition of compound **1**.

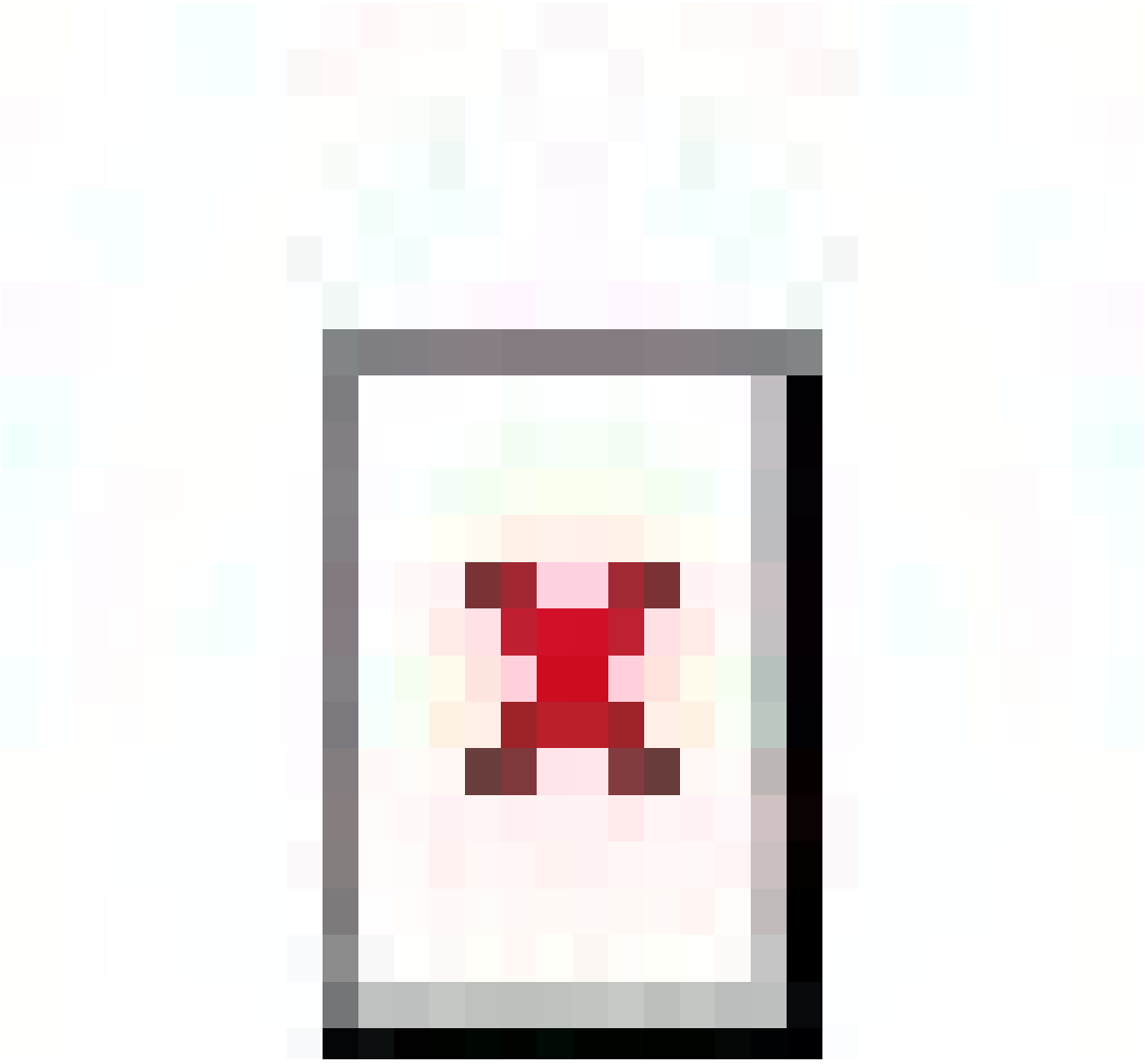

Figure S 47. Fitting parameters associated with the $^4F_{9/2} \rightarrow {}^6H_{13/2}$ transition of compound **1**.

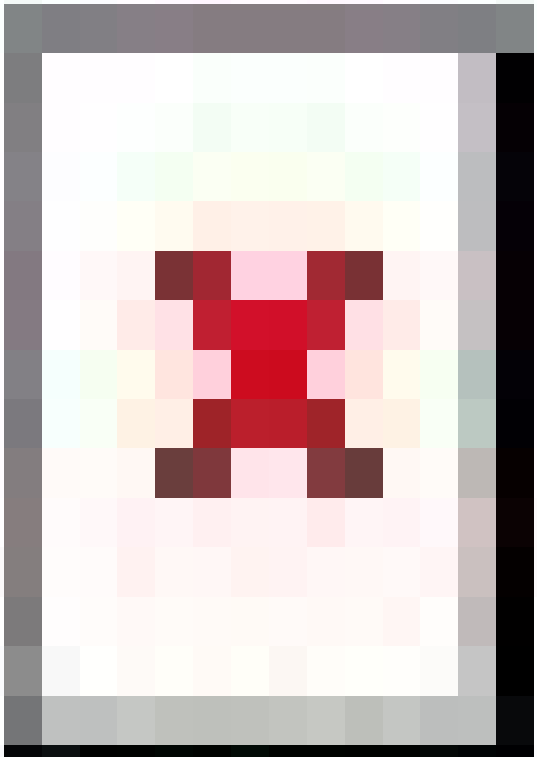

Figure S 48. Fitting parameters associated with the $^4F_{9/2} \rightarrow {}^6H_{11/2}$ transition of compound **1**.

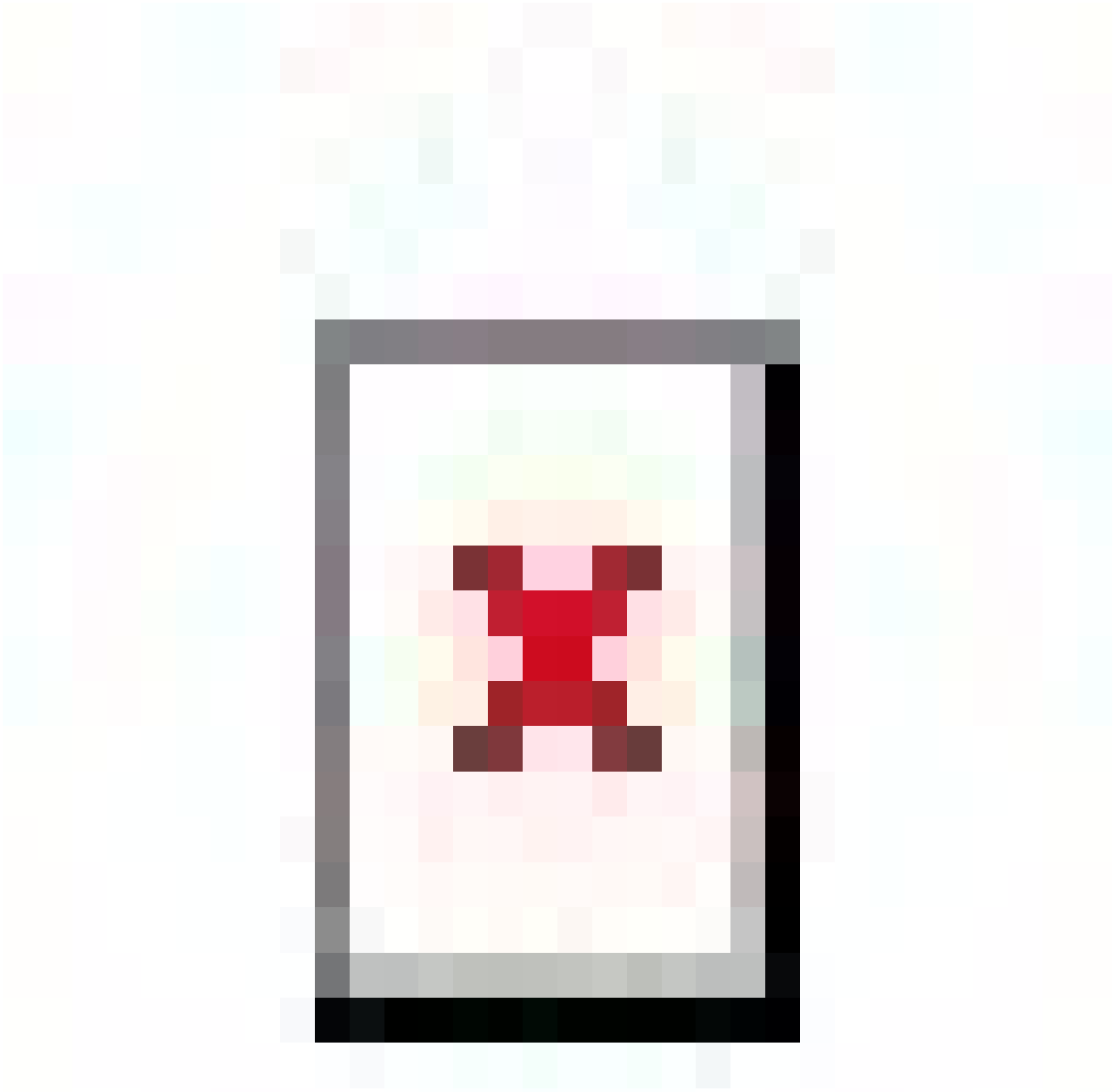

Figure S 49. Fitting parameters associated with the $^4F_{9/2} \rightarrow {}^6H_{9/2}$ and $^4F_{9/2} \rightarrow {}^6F_{11/2}$ transitions of compound **1**.

Table S15. Crystal field splitting energies of the $^6H_{13/2}$ state estimated from the PL spectrum of compound **1** obtained at 2.4 K.

KD	Peak position (nm/cm^{-1})	Relative energy (cm^{-1})	Energy difference (cm^{-1})
1	573.8/17427.7	0	0
2	575.4/17379.2	48.5	48.5
3	576.8/17337	90.7	42.2
4	578.1/17298	129.7	39
5	578.9/17274	153.7	24
6	580.5/17226.5	201.2	47.5
7	582.5/17167.4	260.3	59.1

Table S16. Crystal field splitting energies of the $^6H_{11/2}$ state estimated from the PL spectrum of compound **1** obtained at 2.4 K.

KD	Peak position (nm/cm^{-1})	Relative energy (cm^{-1})	Energy difference (cm^{-1})
1	662.3/15098.9	0	0
2	664.8/15042.1	56.8	56.8
3	666.2/15010.5	88.4	31.6
4	667.2/14988	110.9	22.5
5	668.1/14967.8	131.1	20.2
6	669.5/14936.5	162.4	31.3

Table S17. Crystal field splitting energies of the $^6H_{9/2}$ state estimated from the PL spectrum of compound **1** obtained at 2.4 K.

KD	Peak position (nm/cm^{-1})	Relative energy (cm^{-1})	Energy difference (cm^{-1})
1	750.7/13320.9	0	0
2	752.9/13281.9	39	39
3	754.3/13257.3	63.6	24.6
4	756.9/13211.8	109.1	45.5
5	758.7/13180.4	140.5	31.4

S8. Computational studies

Multistep procedure to compute the magnetic properties of 1

Using the structure with optimized H-positions, a series of Restricted Open Shell Hartree-Fock (ROHF) calculations was performed which results in reliable f-orbitals for the following Complete Active Space Spin Orbit Configuration Interaction (CASOCI) calculation.

In a first step, Dy(III) is replaced to Gd(III) and a ROHF calculation (a=1, b=2) is performed including scalar-relativistic effects on a DKH2 level of theory. An all electron x2c-TZVPall basis was employed for Gd(III) while a def2-TZVP basis was used for all other atoms. Here, the energy was converged to 10^{-7} E_h.

In a second step, Gd(III) was replaced to Dy(III) using the same basis x2c-TZVPall and the same ROHF calculation was performed, now with the Roothaan-parameters a = 238/243 and b = 308/243. In the last step, DKH2 was changed to DKH4, and tighter convergence criteria were set where the energy was converged to 10^{-8} E_h and the density was converged to 10^{-7}. Afterwards, the necessary integrals were calculated using a Spin-Orbit mean Field (SOMF) approach, before the full Hamiltonian (including SOC) was diagonalized using a Block-Davidson diagonalization to get explicit wavefunctions for the lowest 200 states.

To analyse the PL-spectra of the lowest $^6H_{15/2}$ multiplet, it cannot be assumed that the compositions of the $^4F_{9/2}$ state are necessarily the correct ones due to the accuracy of the calculations. Therefore, the energies and oscillator strengths of the 5 KDs of $^4F_{9/2}$ are averaged (Figure S 50). Furthermore, the energies of the $^4F_{9/2}$ states is shifted by -3391.5 cm^{-1} to align

with the transition into the lowest KD of the $^6H_{15/2}$ state. Lastly, the intensities of the transition are convoluted with gaussians (σ = 10 cm^{-1}) and normalized to the intensity of the transition into the ground state KD.

Table S18. Experimental and calculated CF splitting energies and m_J composition of the $^6H_{13/2}$, $^6H_{11/2}$, and $^6H_{9/2}$ multiplets of Dy(III) in compound **1**. The m_J contributions ≥ 5% for each KD are given. The axes system is taken from the lowest KD of the $^6H_{15/2}$ ground state. The m_J composition of the $^6F_{9/2}$ state is also given at the end of the Table.

$^{2S+1}L_J$	Exp. position (cm^{-1})	Exp./ CASOCI energy (cm^{-1})	Relative Energies Exp./CASOCI	m_J composition
$^6H_{13/2}$	17427.7	3563.1/3509.5	0.0/0.0	54.0%|±13/2>+40.2%|±11/2>
	17379.2	3611.6/3546.0	48.5/36.5	9.9%|±9/2>+11.5%|±7/2>+16.4%|±5/2>+28.7%|±3/2>+27.9%|±1/2>
	17337	3653.8/3577.6	90.7/68.1	12.3%|±13/2>+16.4%|±11/2>+46.3%|±9/2>+12.3%|±5/2>+7.7%|±1/2>
	17298	3692.8/3600.7	129.7/91.2	5.3%|±13/2>+6.1%|±9/2>+36.5%|±7/2>+15.1%|±5/2>+18.6%|±3/2>+15.7%|±1/2>
	17274	3716.8/3638.0	153.7/128.5	8.7%|±13/2>+8.4%|±11/2>+19.1%|±7/2>+18.6%|±5/2>+16.5%|±3/2>+24.7%|±1/2>
	17226.5	3764.3/3655.5	201.2/146.0	8.1%|±13/2>+10.8%|±11/2>+23.3%|±5/2>+30.5%|±3/2>+22.0%|±1/2>
	17167.4	3823.4/3727.0	260.3/217.5	7.1%|±13/2>+20.6%|±11/2>+29.6%|±9/2>+25.3%|±7/2>+12.9%|±5/2>
$^6H_{11/2}$	15098.9	5891.9/5998.2	0.0/0.0	32.9%|±11/2>+48.5%|±9/2>+9.8%|±7/2>
	15042.1	5948.7/6035.1	56.8/36.9	7.8%|±11/2>+5.2%|±9/2>+15.6%|±7/2>+33.6%|±5/2>+24.0%|±3/2>+13.8%|±1/2>
	15010.5	5980.3/6067.0	88.4/68.8	13.0%|±11/2>+33.6%|±7/2>+7.4%|±5/2>+20.6%|±3/2>+22.6%|±1/2>
	14988	6002.8/6097.4	110.9/99.2	14.0%|±11/2>+6.4%|±7/2>+16.9%|±5/2>+15.2%|±3/2>+42.6%|±1/2>

	14967.8	6023/6123.2	131.1/125.0	26.0%|±11/2>+35.0%|±9/2>+22.1%|±7/2>+5.1%|±5/2>+6.0%|±3/2>+5.7%|±1/2>
	14936.5	6054.3/6162.8	162.4/164.6	6.3%|±11/2>+12.4%|±7/2>+34.0%|±5/2>+30.9%|±3/2>+12.8%|±1/2>
$^6H_{9/2}$	13320.9	7669.9/7916.2	0.0/0.0	32.9%|±9/2>+50.7%|±7/2>+7.9%|±5/2>
	13281.9	7708.9/7949.4	39.0/33.2	9.4%|±9/2>+5.1%|±7/2>+23.6%|±5/2>+36.7%|±3/2>+25.2%|±1/2>
	13257.3	7733.5/7994.1	63.6/77.9	7.7%|±9/2>+5.8%|±7/2>+28.1%|±5/2>+13.2%|±3/2>+45.2%|±1/2>
	13211.8	7779/8024.5	109.1/108.3	36.7%|±9/2>+36.3%|±7/2>+19.5%|±5/2>
	13180.4	7810.4/8075.8	140.5/159.6	13.4%|±9/2>+20.9%|±5/2>+41.0%|±3/2>+22.7%|±1/2>
$^4F_{9/2}$	-	20990.8/24238.5	0.0/0.0	22.8%|±9/2>+12.3%|±7/2>+12.7%|±5/2>+8.7%|±3/2>+43.4%|±1/2>
	-	-/24306.5	-/68.0	38.7%|±9/2>+14.4%|±5/2>+22.6%|±3/2>+23.9%|±1/2>
	-	-/24358.0	-/119.5	5.8%|±9/2>+32.3%|±7/2>+5.4%|±5/2>+40.6%|±3/2>+15.9%|±1/2>
	-	-/24443.2	-/204.7	28.9%|±9/2>+31.9%|±7/2>+22.6%|±5/2>+14.0%|±3/2>
	-	-/24511.4	-/272.9	23.0%|±7/2>+45.0%|±5/2>+14.0%|±3/2>+14.2%|±1/2>

Table S19. Calculated crystal-field parameters for the Dy(III) compound **1**.

k	*q*	B(*k*,*q*)
2	-2	-0.53831963118264E-01
2	-1	0.27005370583707E+01
2	0	0.10317198013465E+00
2	1	0.25816039305738E+00
2	2	0.13261051051435E+00
4	-4	-0.10266971013527E-02
4	-3	-0.25341611940877E-01
4	-2	0.79757883215711E-02
4	-1	0.31142022010069E-01
4	0	-0.23814518211352E-02
4	1	0.71544344007480E-02

4	2	-0.22511695969898E-01
4	3	-0.11430319477058E-01
4	4	-0.12617054602491E-02
6	-6	0.45337036466922E-04
6	-5	-0.18238397951587E-04
6	-4	-0.65839785067384E-04
6	-3	-0.19017746219840E-03
6	-2	0.35768808020879E-04
6	-1	-0.72928738835575E-04
6	0	-0.23195420955679E-04
6	1	-0.63920481886426E-05
6	2	-0.13817657075751E-03
6	3	-0.11730477959608E-03
6	4	0.90536546150828E-04
6	5	0.31731183019278E-04
6	6	-0.39349053386612E-04

Table S20. Zero Field splitting and calculated g-Tensors for the lowest $^{6}H_{15/2}$-multiplet.

Energy	gx	gy	gz
0	0.134321	0.194512	18.87435
45.712	0.753446	1.343725	16.72981
79.963	1.868022	3.210863	12.97962
95.192	3.447819	4.843135	10.07741
119.44	0.703788	0.800476	13.2093
164.892	0.055595	0.180222	17.15089
197.953	0.023147	0.095372	19.42313
388.181	0.001773	0.002804	19.79286

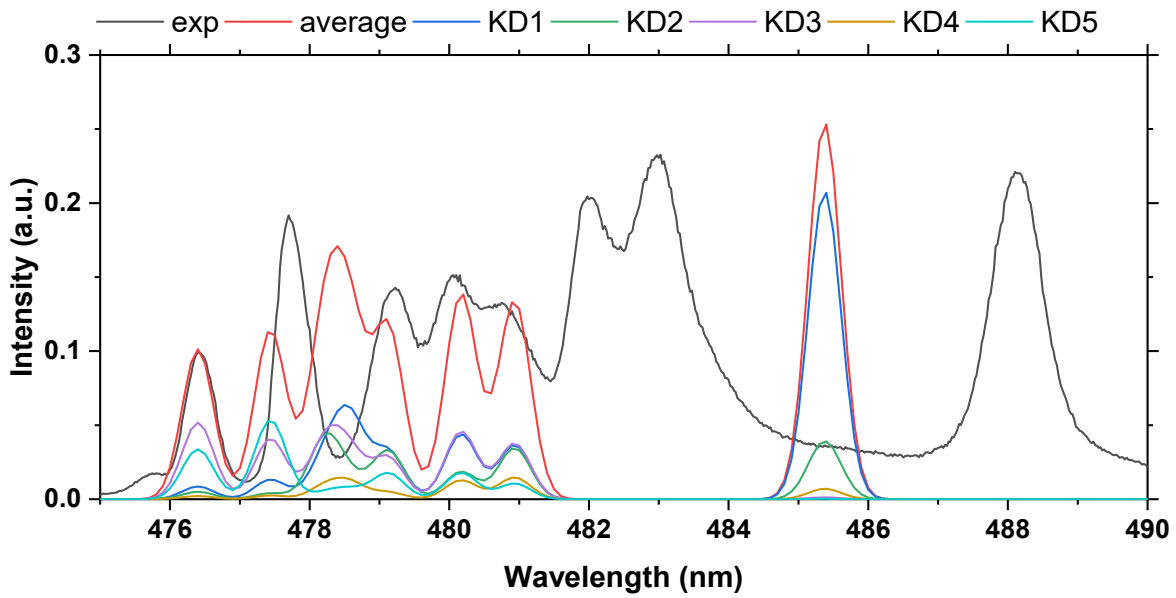

Figure S 50. Contribution of each KD of the $^4F_{9/2}$ multiplet to the calculated oscillator strengths. Here all excited state energies are shifted to the experimental value. It can be clearly seen that the relative intensities are not reproduced considering emission from a single calculated KD.

Table S21. Coordinates used for the calculation of magnetic properties.

Atom	X	Y	Z
Dy	4.471	12.4609	12.7308
O	3.9549	13.9063	14.5082
O	5.9724	14.2662	12.474
O	3.1283	14.1623	11.7684
O	4.0162	10.3146	11.9628
O	5.0345	12.4411	10.3991
O	6.6436	11.5567	12.6448
O	2.1671	11.959	13.1891
O	4.6949	11.2578	14.7236
N	4.3784	15.0228	9.5075
H	3.908604	14.89395	10.47092
H	5.098772	14.26783	9.545624
C	3.6103	13.7674	15.7184
C	4.2871	11.3999	15.9107
C	7.7194	11.9462	12.1287
C	4.3667	9.636	10.9677
C	1.1497	12.6766	13.3155
C	2.6651	16.0601	15.6312
H	2.643837	15.92929	14.55213
C	3.118	15.0083	16.4133
C	5.32	11.4719	9.6058
C	3.6992	12.5621	16.4287
H	3.362854	12.54058	17.46349

C	7.1659	14.3552	12.0328
C	6.931	12.9224	8.3788
H	7.091728	13.43772	9.329271
C	1.03	14.0124	12.8586
H	0.137086	14.56762	13.14269
C	3.9457	14.788	7.073
H	3.150992	14.56713	6.344423
H	4.725449	14.02223	6.932743
C	3.1636	15.1837	17.7957
H	3.546734	14.3849	18.43303
C	8.0401	13.2905	11.8513
H	9.045449	13.50124	11.48827
C	8.7244	10.8829	11.7466
H	8.444135	10.47603	10.76138
H	8.682195	10.0554	12.46768
H	9.749454	11.27164	11.67747
C	2.0286	14.6904	12.1789
C	3.3656	14.6706	8.4678
H	2.519312	15.36096	8.608641
H	3.019482	13.65383	8.695082
C	5.0165	10.137	9.8337
H	5.327106	9.413972	9.081256
C	4.528	16.1781	6.8399
H	5.00075	16.23019	5.847661
H	3.713686	16.92506	6.839759
C	2.7675	16.3821	18.3731
H	2.826952	16.50621	19.45667
C	1.8942	16.17	11.9625
C	6.0647	11.8337	8.3549
C	7.6189	15.7504	11.6745
C	4.4988	10.2268	16.8434
H	5.576795	10.12188	17.04524
H	4.171258	9.301502	16.34778
H	3.971182	10.34402	17.79891
C	3.0409	16.9527	12.1558
H	3.978582	16.45288	12.40769
C	7.0765	16.829	12.3674
H	6.384373	16.62025	13.18493
C	0.68	16.7955	11.6731
H	-0.21824	16.19573	11.51488
C	4.1015	8.1509	11.0331
H	3.05593	7.980254	11.32824
H	4.731283	7.717231	11.82582
H	4.308451	7.632316	10.08804
C	5.5371	16.5272	7.9255
H	6.417878	15.86966	7.84747
H	5.903717	17.55807	7.808391
C	8.5058	15.9897	10.6258
H	8.936177	15.15413	10.07142
C	5.9176	11.1179	7.1623
H	5.234505	10.26923	7.112317

C	4.9292	16.3904	9.3058
H	5.661379	16.57467	10.10186
H	4.090833	17.08894	9.447634
C	2.9637	18.3409	12.0885
H	3.853486	18.9455	12.27444
C	-0.0182	12.0803	14.0749
H	0.218728	12.10685	15.15052
H	-0.13619	11.02516	13.79255
H	-0.95858	12.62331	13.9114
C	2.2539	17.2536	16.2084
H	1.892297	18.06428	15.57146
C	2.3085	17.4167	17.5777
H	1.995575	18.35936	18.03297
C	7.4265	18.1345	12.0387
H	7.019382	18.97016	12.6115
C	1.754	18.9475	11.7897
H	1.691683	20.03655	11.72925
C	0.623	18.184	11.5729
H	-0.32525	18.66911	11.33124
C	7.627	13.3075	7.2428
H	8.321554	14.14913	7.283296
C	8.2896	18.3661	10.9843
H	8.557561	19.38992	10.71258
C	8.832	17.3026	10.2703
H	9.514703	17.49088	9.439339
C	6.6123	11.5215	6.0252
H	6.477068	10.9668	5.093568
C	7.4575	12.5982	6.0621
H	8.002444	12.89754	5.163897

Formulas used to calculate QTM-times:[15–18]

Yin *et al.*:
$$\tau_{QTM} = \frac{h}{\mu_B B} \cdot \frac{sqrt(g_x^2 + g_y^2 + g_z^2)}{g_x^2 + g_y^2} \qquad \text{Eq. S5}$$

Prokov'ef and Stamp:
$$\tau_{QTM} = \frac{h}{\mu_B B} \cdot \frac{g_z}{2sqrt(2\pi) \cdot (g_x^2 + g_y^2)} \qquad \text{Eq. S6}$$

S9. Molecular structures of $[Dy(L)_4]^-$ complexes discussed in the literature

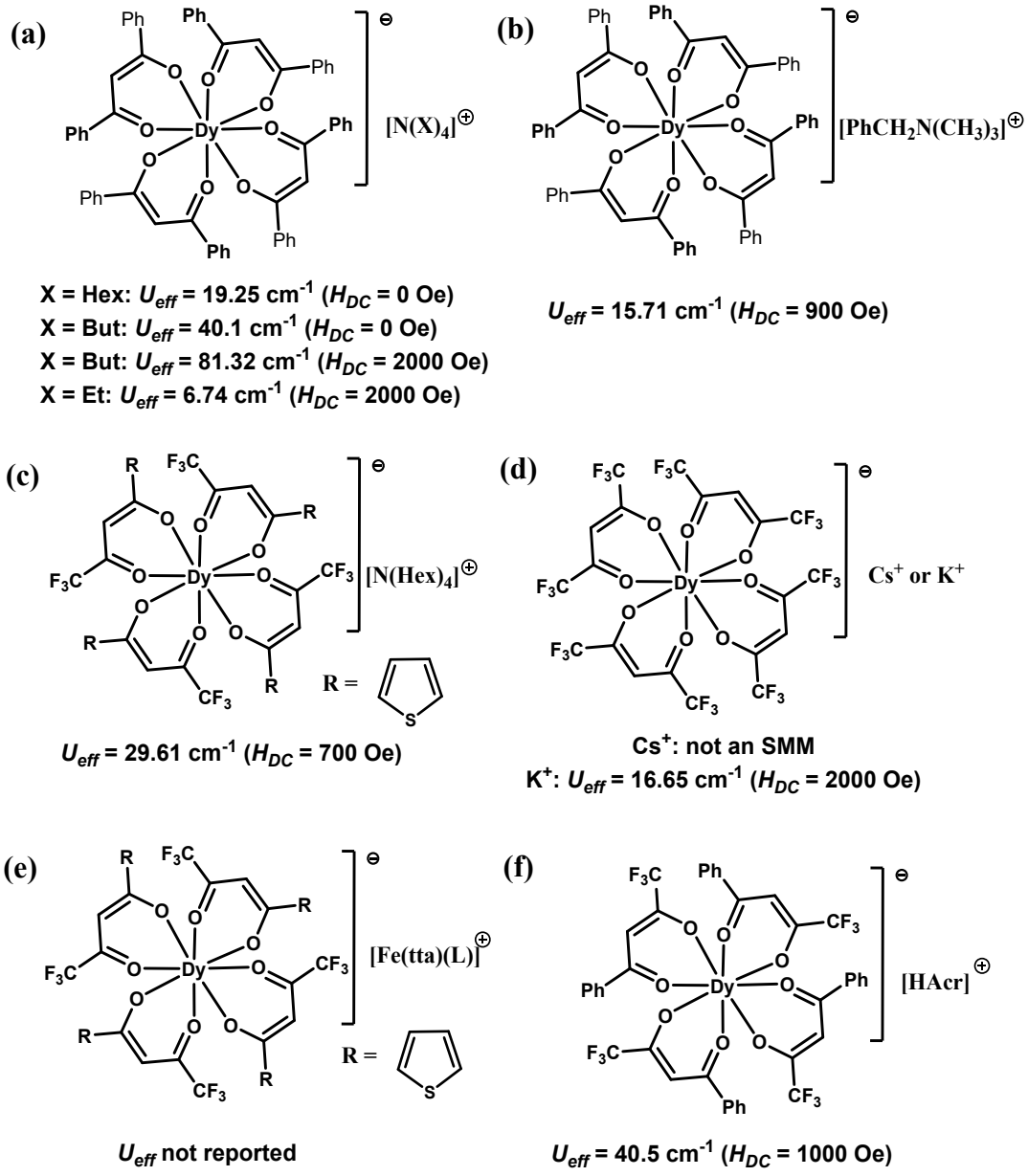

Figure S 51. Molecular structures of tetrakis-β-diketone compounds and energy barriers (U_{eff}) for magnetization relaxation associated with them.

S10. References

[1] O. V. Dolomanov, L. J. Bourhis, R. J. Gildea, J. A. K. Howard, H. Puschmann, "*OLEX2*: a complete structure solution, refinement and analysis program" *J Appl Crystallogr* **2009**, *42*, 339–341.

[2] G. M. Sheldrick, "*SHELXT*– Integrated space-group and crystal-structure determination" *Acta Crystallogr A Found Adv* **2015**, *71*, 3–8.

[3] G. M. Sheldrick, “Crystal structure refinement with*SHELXL*” *Acta Crystallogr C Struct Chem* **2015**, *71*, 3–8.
[4] N. Kofod, R. Arppe-Tabbara, T. J. Sørensen, “Electronic Energy Levels of Dysprosium(III) ions in Solution. Assigning the Emitting State and the Intraconfigurational 4f–4f Transitions in the Vis–NIR Region and Photophysical Characterization of Dy(III) in Water, Methanol, and Dimethyl Sulfoxide” *J. Phys. Chem. A* **2019**, *123*, 2734–2744.
[5] Z.-F. Li, L. Zhou, J.-B. Yu, H.-J. Zhang, R.-P. Deng, Z.-P. Peng, Z.-Y. Guo, “Synthesis, Structure, Photoluminescence, and Electroluminescence Properties of a New Dysprosium Complex” *J. Phys. Chem. C* **2007**, *111*, 2295–2300.
[6] J. Manzur, P. Fuentealba, Y. Gil, J. Pérez-Obando, J. Morales Alfaro, A. I. Vega Carvallo, D. Aravena, R. C. D. Santana, A. N. Carneiro Neto, E. Spodine, “Tuning the Emission of Homometallic Dy^{III} , Tb^{III} , and Eu^{III} 1-D Coordination Polymers with 2,6-Di(1 *H* -1,2,4-triazole-1-yl-methyl)-4-R-phenoxo Ligands: Sensitization through the Singlet State” *Inorg. Chem.* **2023**, *62*, 19195–19207.
[7] L. Reddy, “A Review of the Efficiency of White Light (or Other) Emissions in Singly and Co-Doped Dy3+ Ions in Different Host (Phosphate, Silicate, Aluminate) Materials” *J Fluoresc* **2023**, *33*, 2181–2192.
[8] D. Serrano, S. K. Kuppusamy, B. Heinrich, O. Fuhr, D. Hunger, M. Ruben, P. Goldner, “Ultra-narrow optical linewidths in rare-earth molecular crystals” *Nature* **2022**, *603*, 241–246.
[9] M. Runowski, N. Stopikowska, S. Lis, “UV-Vis-NIR absorption spectra of lanthanide oxides and fluorides” *Dalton Trans.* **2020**, *49*, 2129–2137.
[10] A. G. Bispo-Jr, L. Yeh, D. Errulat, D. A. Gálico, F. A. Sigoli, M. Murugesu, “Improving the performance of β-diketonate-based Dy^{III} single-molecule magnets displaying luminescence thermometry” *Chem. Commun.* **2023**, *59*, 8723–8726.
[11] J. Legendziewicz, M. Borzechowska, “Heteronuclear Eu:Cu trichloroacetate and its polynuclear Eu analogue; their spectroscopy and magnetism” *Journal of Alloys and Compounds* **2000**, *300–301*, 353–359.
[12] J. Huang, J. Loriers, P. Porcher, G. Teste De Sagey, P. Caro, C. Levy-Clement, “Crystal field effect and paramagnetic susceptibility of Na5Eu(MoO4)4 and Na5Eu(WO4)4” *The Journal of Chemical Physics* **1984**, *80*, 6204–6209.
[13] P. Caro, P. Porcher, “The paramagnetic susceptibility of C-type europium sesquioxide” *Journal of Magnetism and Magnetic Materials* **1986**, *58*, 61–66.
[14] L. Thompson, J. Legendziewicz, J. Cybinska, L. Pan, W. Brennessel, “Structure, photophysics and magnetism of a europium mixed complex, Eu(HFAA)3bipy.H2O, in the solid state and solution” *Journal of Alloys and Compounds* **2002**, *341*, 312–322.
[15] B. Yin, C.-C. Li, “A method to predict both the relaxation time of quantum tunneling of magnetization and the effective barrier of magnetic reversal for a Kramers single-ion magnet” *Phys. Chem. Chem. Phys.* **2020**, *22*, 9923–9933.
[16] N. V. Prokof’ev, P. C. E. Stamp, “Quantum relaxation of magnetisation in magnetic particles” *J Low Temp Phys* **1996**, *104*, 143–209.
[17] N. V. Prokof’ev, P. C. E. Stamp, “Theory of the spin bath” *Rep. Prog. Phys.* **2000**, *63*, 669–726.
[18] F. Luis, M. J. Martínez-Pérez, O. Montero, E. Coronado, S. Cardona-Serra, C. Martí-Gastaldo, J. M. Clemente-Juan, J. Sesé, D. Drung, T. Schurig, “Spin-lattice relaxation via quantum tunneling in an Er 3 + -polyoxometalate molecular magnet” *Phys. Rev. B* **2010**, *82*, 060403.